



RESEARCH ARTICLE

10.1002/2015SW001238

Key Points:

- Poynting flux from DMSP were compared with modeled Joule heat in GEM-CEDAR challenge
- Physics-based and empirical models were evaluated for the first time
- Empirical model shows weaker maximum Poynting flux than observation and most physics-based models

Correspondence to:

L. Rastätter,
Lutz.Rastaetter@nasa.gov

Citation:

Rastätter L., et al. (2016), GEM-CEDAR challenge: Poynting flux at DMSP and modeled Joule heat, *Space Weather*, 14, 113–135, doi:10.1002/2015SW001238.

Received 11 JUN 2015

Accepted 3 JAN 2016

Accepted article online 23 JAN 2016

Published online 18 FEB 2016

GEM-CEDAR challenge: Poynting flux at DMSP and modeled Joule heat

Lutz Rastätter¹, Ja Soon Shim^{1,2}, Maria M. Kuznetsova¹, Liam M. Kilcommons³, Delores J. Knipp^{3,4}, Mihail Codrescu⁵, Tim Fuller-Rowell⁵, Barbara Emery⁴, Daniel R. Weimer⁶, Russell Cosgrove⁷, Michael Wiltberger⁴, Joachim Raeder⁸, Wenhui Li⁸, Gábor Tóth⁹, and Daniel Welling⁹

¹Community-Coordinated Modeling Center, NASA Goddard Space Flight Center, Greenbelt, Maryland, USA, ²IACS, Catholic University of America, Washington, District of Columbia, USA, ³Colorado Center for Astrodynamic Research, University of Colorado Boulder, Boulder, Colorado, USA, ⁴High Altitude Observatory, National Center for Atmospheric Research, Boulder, Colorado, USA, ⁵Space Weather Prediction Center, National Oceanic and Atmospheric Administration, Boulder, Colorado, USA, ⁶Virginia Tech, Blacksburg, Virginia, USA, ⁷SRI International, Menlo Park, California, USA, ⁸Space Sciences Center, University of New Hampshire, Durham, New Hampshire, USA, ⁹School of Engineering, University of Michigan, Ann Arbor, Michigan, USA

Abstract Poynting flux into the ionosphere measures the electromagnetic energy coming from the magnetosphere. This energy flux can vary greatly between quiet times and geomagnetic active times. As part of the Geospace Environment Modeling-coupling energetics and dynamics of atmospheric regions modeling challenge, physics-based models of the 3-D ionosphere and ionospheric electrodynamic solvers of magnetosphere models that specify Joule heat and empirical models specifying Poynting flux were run for six geomagnetic storm events of varying intensity. We compared model results with Poynting flux values along the DMSP-15 satellite track computed from ion drift meter and magnetic field observations. Although being a different quantity, Joule heat can in practice be correlated to incoming Poynting flux because the energy is dissipated primarily in high latitudes where Poynting flux is being deposited. Within the physics-based model group, we find mixed results with some models overestimating Joule heat and some models agreeing better with observed Poynting flux rates as integrated over auroral passes. In contrast, empirical models tend to underestimate integrated Poynting flux values. Modeled Joule heat or Poynting flux patterns often resemble the observed Poynting flux patterns on a large scale, but amplitudes can differ by a factor of 2 or larger due to the highly localized nature of observed Poynting flux deposition that is not captured by the models. In addition, the positioning of modeled patterns appear to be randomly shifted against the observed Poynting flux energy input. This study is the first to compare Poynting flux and Joule heat in a large variety of models of the ionosphere.

1. Introduction

Many ionospheric parameters are of critical importance to the correct specification and forecasting of the ionosphere. Models of the ionosphere include first-principles models [Schunk *et al.*, 2002], coupled magnetosphere-ionosphere models [Raeder *et al.*, 2001a; Wiltberger *et al.*, 2004; Wang *et al.*, 2005; Tóth *et al.*, 2005] and atmospheric empirical models such as the International Reference Ionosphere [Bilitza and Reinisch, 2008]. Empirical models also specify crucial driver or input parameters that affect the ionosphere such as the electrodynamic and Joule heat [Weimer, 2005a], precipitation patterns [Newell *et al.*, 2010], or Poynting flux [Cosgrove *et al.*, 2014]. Empirical models of the electrodynamic are used as drivers by many other physics-based models, such as the CTIPE model [Codrescu *et al.*, 2000; Millward *et al.*, 2001] and the TIE-GCM model [Wang *et al.*, 1999].

The GEM-CEDAR challenge was defined by the Geospace Environment Modeling (GEM) and the coupling energetics and dynamics of atmospheric regions (CEDAR) communities during the 2010 GEM and CEDAR workshops. In this joint challenge the observation and modeling of auroral boundaries and the energy flux from the magnetosphere into the ionosphere are being studied.

The Poynting flux measures the electromagnetic energy transmitted between the magnetosphere and the ionosphere. This energy flux is negative when energy enters the ionosphere and positive when electromagnetic energy flows out of the ionosphere. The inflowing energy dominates throughout all events, except for

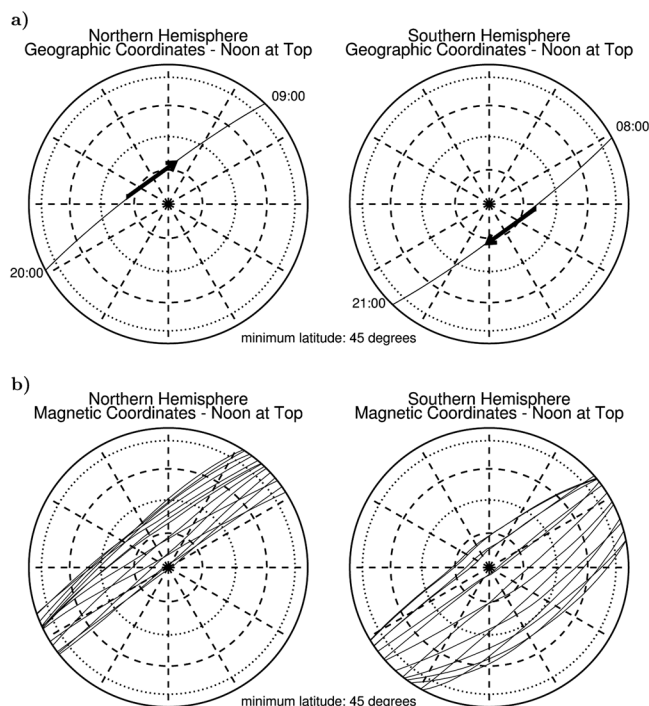


Figure 1. DMSP-F15 passes for event 1 (30 August 2005) relative to (a) geographic and (b) magnetic poles. Passes are shown in coordinates rotated with noon local time on top within 45° of the poles. In geographic coordinates, passes in the north start at 20:00 local time and end at 9:00 local time (with arrow showing direction of satellite motion toward the morning side). Passes in the south start at 08:00 local time and end at 21:00 local time (arrow is pointing to the evening side). In geomagnetic coordinates, the spread of the orbits during the full day and the local time distribution of the start and end positions is wider in the south than the north due to the southern magnetic pole's larger distance from the geographic pole. Orbits for the other events can differ by up to 1.5 h in local time (for example, passes on event 2 on 15 December 2003 start at 22:30 and end at 10:30 in the north in geographic coordinates and start at 9:30 and end at 22:30 in the Southern Hemisphere).

short time intervals of back and forth fluctuations. The Defense Meteorological Satellite Program (DMSP) satellites have been monitoring conditions at an altitude of about 850 km over more than 2 decades. Electric and magnetic field measurements from DMSP satellites can be used to calculate Poynting flux along the satellite track [Huang and Burke, 2004; Knipp et al., 2011], and thus, we can estimate the amount of electromagnetic energy transmitted into the ionosphere. Energy deposited into the ionosphere through electromagnetic fields get dissipated into Joule heat by the ionospheric closure currents in finite ionospheric conductivity. Only in very limited cases when magnetic flux tubes are bounded by equipotential surfaces, this Joule dissipation occurs locally and one may use the Poynting flux instead of its divergence to estimate Joule heat [Richmond, 2010]. In general, however, electromagnetic energy will travel throughout the ionosphere and may lead to Joule heat in midlatitudes or near the equator, whereas the Poynting flux energy is deposited from the magnetosphere in high latitudes. Especially gradients in Pedersen and Hall conductances break the assumption that Poynting flux inflow at the top side of the ionosphere equals Joule heat dissipated locally (either height-integrated or along magnetic flux tubes) [Vanhamäki et al., 2012].

We expect that Joule heat will still be generated locally with a high degree of correlation to the incoming energy. The rise of the plasma and neutral temperatures as a result of Joule heat leads to local expansion of the thermosphere and increased atmospheric drag on low-earth orbiting satellites, and thus, the correct specification of Joule heat is essential for space weather applications [Deng and Ridley, 2007]. We are here reporting on the results for six storm events defined by GEM-CEDAR and have collected Joule heat results from two three-dimensional ionosphere-thermosphere models, the ionospheric electrodynamics of three global magnetosphere models, and two empirical models of Joule heat and Poynting flux. We begin by describing the observations in the following chapter. Then we describe the models, the analysis and results.

2. Satellite Observations

The events selected for this study have Defense Meteorological Satellite Program (DMSP) observations of magnetic and electric fields from the DMSP-SF15 satellite that were of sufficient quality to calculate Poynting flux values [Knipp et al., 2011]. Poynting flux values ($\mathbf{S} = \mathbf{E} \times \delta\mathbf{B}/\mu_0$) were calculated from cross-track plasma velocities (measured by the Ion Drift Meter) and along-track velocities (obtained from the Retarding Potential Analyzer, RPA) [Rich and Hairston, 1994] which are converted to electric field using the International Geophysical Reference Field model for the magnetic background field and magnetic field observations

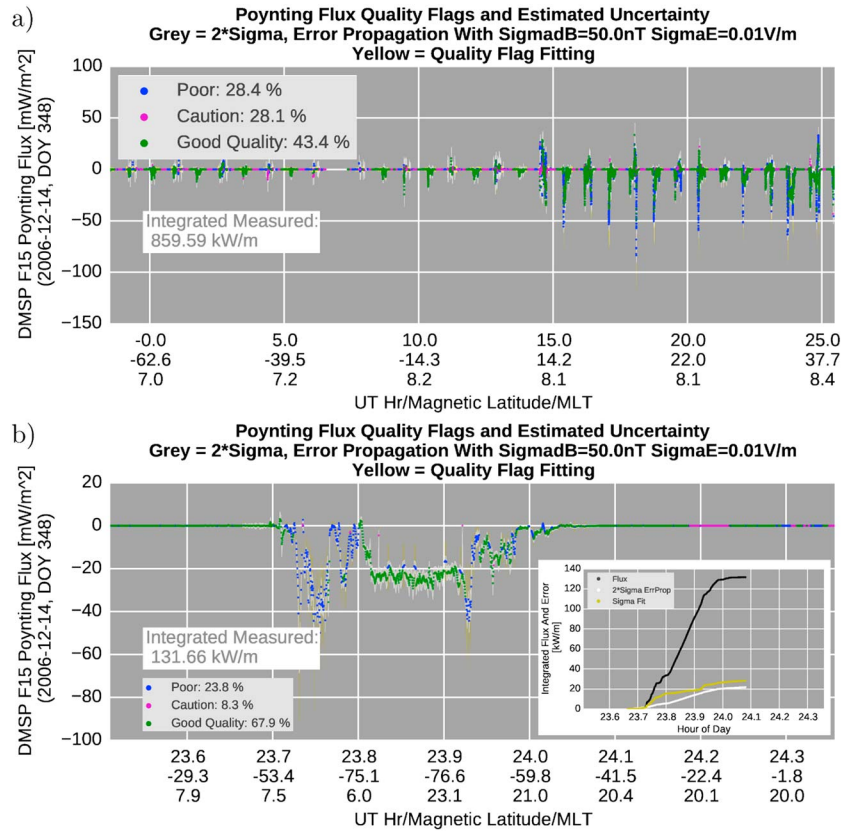


Figure 2. DMSP observation of Poynting flux and associated errors for 14 December 2006: (a) daily plot of all passes with percentages of “good quality” data (green dots), “caution” (purple dots) and “poor” (blue dots), (b) 1 s observation data of the last pass of the day (from about 23:30 UT on 14 December 2006 to 0:15 UT the next day) with status flags mentioned above and error bars: white for “good quality” data indicating a 2 sigma error level from instrument accuracy information and yellow indicating error fit for data with “caution” or “poor” quality flags (derived from statistical analysis from adjacent measurements). Inset: integration of Poynting flux values (black) and errors (white: 2*sigma error, yellow: sigma fit) within 45° of the magnetic pole.

$\delta \mathbf{B} = \mathbf{B}_{\text{meas}} - \mathbf{B}_{\text{IGRF}}$ [Huang and Burke, 2004]. The results are filtered using high-order polynomials to adjust for baseline shifts during each half orbit over the auroral zone (i.e., to ensure that integrated electric potentials from the filtered observations return to the same potential level after a pass through the auroral zone).

The DMSP-F15 satellite orbits from the evening sector into the morning sector in the Northern Hemisphere on a Sun-synchronous orbit so that the satellite reappears at the same position every orbit (in terms of latitude and local time angle as seen from the geographic pole). Figure 1 shows the orbits for a full day (29 October 2003) as an example with the geographic pole in the center of each hemisphere (a) and the magnetic pole in the center (b). As the magnetic poles rotate underneath the orbiting satellite the resulting orbits cover a range of local times as opposed to encountering the same local time at a given latitude in geographic coordinates. Due to the Sun-synchronous nature of the orbit, the arrangement of passes in local time is similar for all the events in this study.

2.1. Measured Poynting Flux Uncertainty (σ_{S_z})

Using the formula (equation (A1) in Appendix A)

$$\sigma(S_z) = \frac{1}{\mu_0} \left[(\sigma_{dB_x} E_y)^2 + (\sigma_{dB_y} E_x)^2 + (\sigma_{E_x} dB_x)^2 + (\sigma_{E_y} dB_y)^2 \right]^{1/2}, \quad (1)$$

where σ is the uncertainty and typical auroral zone values for E_x , E_y , dB_x , and dB_y calculated from the DMSP observations for the events studied here. We estimate that $\sigma(S_z) \sim 2.5 \text{ mW/m}^2$ if all ion drift data are of good quality. For typical auroral zone Poynting flux values of $\sim 10 \text{ mW/m}^2$, this would suggest an uncertainty of 25%.

Table 1. Event Numbers With Dates, Minimum D_{st} , Maximum K_p and AL Values^a

Number	Event Name	Date and UT Time	Min(D_{st}) (nT)	Max(K_p)	Max AL
1	E.2003.302	29 Oct 2003 06:00 to 30 Oct 2003 06:00	−353	9	2284
2	E.2006.348	14 Dec 2006 11:30 to 16 Dec 2006 00:00	−139	8	4056
3	E.2001.243	31 Aug 2001 00:00 to 1 Sep 2001 00:00	−40	4	959
4	E.2005.243	31 Aug 2005 09:30 to 1 Sep 2005 12:00	−131	7	2063
5	E.2005.135	15 May 2005 00:00 to 16 May 2005 00:00	−247	8+	2051
6	E.2005.190	9 Jul 2005 00:00 to 12 Jul 2005 00:00	−89	8−	2115

^aThe first four events were the four original events on the GEM-2008 challenge [Pulkkinen, 2011; Rastätter et al., 2011]. The last two events were defined for the CEDAR challenge in 2009.

However, there is an additional measurement quality factor to consider in terms of uncertainty: The quality (quality flag) of the ion drift data can take on several values, ranging from: QF1—“useable,” QF2—“use with caution,” and QF3—“do not use.” Additionally, there are data labeled as QF4—“unknown.” Data are labeled as Q4 when the subsecond drift measurements show significant variability. Data with a QF4 label often appear in the cusp region where high variability is to be expected and, thus, may be of acceptable quality. During any given DMSP pass the quality of the ion drift data can change often, with high quality data juxtaposed with lower quality data. This introduces a significant uncertainty in the pass-integrated Poynting flux values, see Figure 2a. We have developed an objective method of assigning relative uncertainty to the point calculations of Poynting flux based on the quality flags. The basis for this assignment comes from analysis of the second-by-second changes in data quality and resultant uncertainty of the Poynting flux values. An example of the uncertainty assignment of a single polar pass is shown in Figure 2b. For each measurement, the associated quality flag in the data was used to specify the error level associated with the observation. Integrated errors for each pass are shown in comparisons of pass-integrated Poynting flux with modeled Joule heat. Single measurement errors are used in comparisons of maximum values in the results section. Only passes with integrated Poynting flux values larger than the error level are included in the skill score averages. We refer to Appendix A for a detailed description of the determination of the errors based on the quality flags that come with the DMSP instrument data.

3. Setup of the Challenge

Negative values of S_z as calculated from DMSP observations indicate that electromagnetic energy is flowing from the magnetosphere into the ionosphere. All models calculate positive values (either as Joule heat or Poynting flux) to indicate that energy is being added to the ionosphere. Thus, in this study we multiply by (−1) the vertical component of the Poynting flux S_z from the observations and use $PF = -S_z$ to facilitate direct comparison with the values obtained from the models. PF data are available on a 1 s cadence from the observations. For the comparison with models we calculate 10 s boxcar averages that are then compared with model results. The satellite moves about 8 km/s, so 10 s translate to scales of about 80 km, similar to the finest resolution in latitude of some of the models ($1^\circ \sim 126$ km). PF values are then compared with Joule heat values that are always positive.

Table 1 lists the six geomagnetic storm events that are used in the study with the strongest values of the geomagnetic activity indices D_{st} , K_p , and AL during each event. Each event covers between 1 day (24 h) and 3 days (72 h) of time and include the onset and main phase of each storm. The events include weaker storms, moderate storms, and two superstorms from solar cycle 23 to cover a wide range of conditions.

4. Simulation Models

The coupled magnetosphere-ionosphere simulation runs that entered the challenge were run with moderate grid resolutions that could also be used in operational (real time) settings [Pulkkinen et al., 2013]. We have three types of models that entered this challenge described below and listed in Table 2:

4.1. Electrodynamics Solvers Coupled to Magnetosphere MHD Models

Magnetosphere magnetohydrodynamic (MHD) models have a coupled electrodynamic potential solver to provide self-consistent boundary conditions at the near-Earth boundary. The global MHD model provides

Table 2. Run Settings Used in Comparisons^a

Model Description	Identifier
SWMF v2011/01/31, coupled with RCM, 1.007 million cells and 1/4 R _E resolution	9_SWMF
OpenGGCM v. 4.0, 1/4 R _E resolution, 270 × 120 × 120 cells	4_OPENGGCM
OpenGGCM v. 4.0, 1/4 R _E resolution 630 × 200 × 300 cells (Events 4 and 5 only)	8_OPENGGCM*
CMIT v. LTR-2.1.5, LFM-MIX, 53 × 48 × 64 cells	2_LFM-MIX
CMIT v. LTR-2.1.5, LFM-MIX-TIEGCM, LFM with 53 × 48 × 64 cells	2_CMIT
TIEGCM v. 1.94, driven by Weimer-2005 electric field	2_TIE-GCM
CTIpe, version 2.0, run at CCMC	1_CTIPE
Weimer 2005 Poynting flux model, submitted by D. Weimer (except for Event 2)	1_WEIMER*
Weimer 2005 Joule heat model, using solar wind and AL index	7_WEIMER
Weimer 2005 Joule heat model, using solar wind only	8_WEIMER
Cosgrove Poynting flux model, version 1.0, using solar wind and AL index	1_Cosgrove
Cosgrove Poynting flux model, version 1.0, using solar wind only	2_Cosgrove

^aModels include the ionosphere electrodynamics outputs of magnetosphere models (SWMF, OpenGGCM, and LFM/CMIT), 3-D ionosphere thermosphere models (TIE-GCM, CTIpe) and empirical models of Poynting flux or Joule heat (WEIMER) and Poynting flux (Cosgrove). (*) Model results were submitted by modeler (i.e., not run at the CCMC).

magnetic field-aligned electric currents that enter the ionosphere. In the ionosphere electrodynamics solver, a conductance model (either fully empirical or derived from ionosphere-thermosphere ion species distributions) is used to derive the height-integrated flow of electric currents and the resulting electric potential distribution. From the potential pattern, the electric field is mapped back along the magnetic field (assumed to be dipolar) to the inner boundary of the MHD to provide plasma flow boundary conditions. From the electrodynamics solver outputs, we use the height-integrated electric current and the electric field to calculate Joule heat rates.

All global magnetosphere models use solar wind data (typically from ACE or Wind) projected to the respective model's upstream boundary to drive the magnetospheric magnetohydrodynamic model and the solar $F_{10.7}$ flux index value to calculate background EUV contributions to the ionospheric conductances in the electrodynamics solver.

From the electrodynamic solutions in the ionosphere we cannot use electric and magnetic fields to calculate Poynting flux since these models only compute an electrostatic potential solution and large-scale current closure through the ionosphere. However, using the ionospheric Pedersen conductance Σ_p and electric field (\mathbf{E}), we can compute the Joule heat ($JH = \Sigma_p \mathbf{E}^2 = \mathbf{J} \cdot \mathbf{E}$) and use it as a proxy for PF assuming that energy deposited into the ionosphere is being dissipated locally.

4.1.1. SWMF (9_SWMF)

The Space Weather Modeling Framework (SWMF) [Tóth *et al.*, 2005, 2012] (<http://csem.engin.umich.edu/swmf/>) run includes the Block-Adaptive Tree-Solarwind Roe-type Upwind Scheme (BATS-R-US) magnetosphere MHD model [Powell *et al.*, 1999; Gombosi *et al.*, 2014] that is coupled to the Rice Convection Model [Wolf *et al.*, 1982; Toffoletto *et al.*, 2003] in the inner magnetosphere and both are coupled to the Ridley Ionosphere Model [Ridley *et al.*, 2004] to provide a representation of the ionospheric electrodynamics and near-Earth boundary conditions.

The magnetosphere was resolved in a grid with 1 million cells providing 1/4R_E resolution near the Earth, inner magnetosphere, and near-Earth magnetotail and 1° in latitude by 2° in longitude resolution in the ionosphere. The magnetosphere simulation box extends from −232R_E in X to +32R_E and from −128R_E to +128R_E in Y and Z . Run parameters are the same as used by the magnetic perturbation study and are described in detail in Pulkkinen *et al.* [2013].

4.1.2. OpenGGCM (4_OPENGGCM, 8_OPENGGCM)

The Open General Geospace Circulation Model (OpenGGCM) [Raeder *et al.*, 1996, 1998, 2001b] simulates the magnetosphere-ionosphere system by employing the CTim ionosphere model [Fuller-Rowell *et al.*, 1996] to provide conductances, an electrodynamic solver to calculate electric potentials and currents as inner boundary conditions for a low-diffusion magnetohydrodynamics model in the magnetosphere.

All the coupled magnetosphere-ionosphere-thermosphere models use solar wind data (density, velocity, and magnetic field) and the solar radiation index $F_{10.7}$ to specify ionospheric composition and conductances.

The OpenGGCM model was run for 4_OPENGGCM at CCMC with $1/4R_E$ resolution near the Earth on a grid of $270 \times 120 \times 120$ cells in a box extending from -300 to 30 in X and -38 to $+38$ in Y and Z .

The 8_OPENGGCM was submitted by the modeler (Wenhui Li) for events 4 and 5 only. The model was run with $630 \times 200 \times 300$ cells in a box extending from -300 to 20 in X and -40 to 40 in Y and Z . The minimum resolution is $0.25 R_E$ in Y and $0.16 R_E$ in Z at the X axis and the grid has a minimum resolution of $0.14 R_E$ in X in the dayside and near the Earth. OpenGGCM has successfully been used to compare DMSP Poynting fluxes due to cusp reconnection by *Li et al.* [2011] for northward interplanetary magnetic field (IMF) conditions.

4.1.3. CMIT (2_LFM-MIX, 2_CMIT)

The Coupled Magnetosphere Ionosphere Thermosphere (CMIT) model [*Wang et al.*, 2004; *Wiltberger et al.*, 2004] combines the Lyon-Fedder-Mobarry magnetosphere model [*Lyon et al.*, 2004], the TIE-GCM ionosphere model [*Roble and Ridley*, 1994; *Wang et al.*, 1999], and the MIX coupler and electrodynamic solver [*Merkin and Lyon*, 2010].

In run 2_LFM-MIX the magnetosphere model and ionosphere solver are run alone, and ionospheric conductances are determined from solar extreme ultraviolet inputs ($F_{10.7}$ index) and field-aligned currents via empirical models [*Wiltberger et al.*, 2009]. Run 2_CMIT also employs the TIE-GCM ionosphere to provide conductances calculated from the height-resolved ionosphere ion composition.

The LFM magnetosphere covers a cylinder of $132 R_E$ radius extending from $-300 R_E$ to $+30 R_E$ in X . Both runs were performed with real-time settings employing 24 processors and the $53 \times 48 \times 64$ cell grid in the magnetosphere providing $0.4 R_E$ radial resolution in the dayside and $2 \times 2^\circ$ in the ionosphere above 45° magnetic latitude.

For more detailed descriptions of these magnetosphere model settings we refer to *Pulkkinen et al.* [2013] and *Rastätter et al.* [2014].

4.2. Physics-Based Model of the Ionosphere

We used results from two stand-alone first-principles models of the ionosphere-thermosphere system, the TIE-GCM and CTIPe models. Both models can either be fed by statistical electrodynamics models providing high-latitude electric fields and low-latitude drifts or coupled to a magnetospheric magnetohydrodynamic model as is done in the CMIT model that runs TIE-GCM. These models provide Joule dissipation rates from electric current density (in A/m) and electric fields:

4.2.1. TIE-GCM (2_TIE-GCM)

The Thermosphere-Ionosphere-Electrodynamics General Circulation Model (TIE-GCM) [*Roble et al.*, 1988; *Richmond et al.*, 1992; *Roble and Ridley*, 1994; *Wang et al.*, 1999] covers the ionosphere from about 97 km to about 500 km altitude in 29 constant pressure layers. Standard resolution is 5° in longitude and latitude and 2 levels per scale height (pressure level) in altitude. The TIE-GCM uses either a *Weimer* [2005a] or *Heelis et al.* [1982] electric field model. In this study, run 2_TIE-GCM was run with model version 1.93 and the *Weimer* [2005a] electric field model.

4.2.2. CTIPe (1_CTIPe)

The Coupled Thermosphere Ionosphere Plasmasphere with Electrodynamics (CTIPe) also resolves the ionosphere from about 80 km to about 500 km altitude. Standard resolution is 18° in longitude, 2° in latitude, and 1 level per scale height (pressure level) in altitude. CTIPe uses solar wind data from ACE in 1 min cadence that are propagated to the nose of the Earth magnetosphere assuming a constant time shift of 30 min, regardless of the solar wind speed.

Both ionosphere models (TIE-GCM and CTIPe) use solar wind data and the Weimer electric potential model as drivers and return the local Joule heat rate as an output. We use the height-integrated Joule heat values for this study. Stand-alone ionosphere models use solar wind data and solar irradiance index values ($F_{10.7}$). Unlike two-dimensional electrostatic potential solvers in the ionosphere, the three-dimensional height-resolved ionosphere models TIE-GCM and CTIPe (and CTim as part of OpenGGCM) take into account neutral winds which may absorb incoming Poynting flux energy as they are being accelerated. During later parts of a storm when magnetospheric driving is weakening, decelerating neutral winds may provide energy for Joule heat through what is known as the “flywheel effect.”

Model settings of the ionosphere are described in more detail in *Shim et al.* [2011]. All the models in this and the previous sections are physics-based (first principles) models and their results are plotted together. Empirical models are described below and are plotted together in separate plots.

4.3. Empirical Models

Two models are able to provide Joule heat and Poynting flux values, the Weimer electrodynamics models [Weimer, 2005a] (Joule heat) and the Cosgrove Poynting flux model (Cosgrove PF or Cosgrove) [Cosgrove et al., 2014]. These models use as inputs solar wind plasma density N , velocity V_x , magnetic field B_y , and B_z in GSM coordinates and the date and time to calculate the tilt of the Earth's magnetic dipole. All of these models come in two flavors, one that uses the AL index as an addition input and one that does not. These empirical models have been recently implemented at the CCMC and can now be run upon request for extended periods of time (see <http://ccmc.gsfc.nasa.gov/changelog/index.php> – Entry for 5 December 2014), and we use results from this implementation in this study (Weimer without AL index input, Cosgrove with and without AL index input).

4.3.1. Weimer (1_WEIMER, 7_WEIMER, and 8_WEIMER)

The Weimer empirical model of Poynting Flux derives values from perturbation electric and magnetic fields, based on Dynamics Explorer-2 observation data (from 1981 to 1983). Weimer [2005b] describes how electric potential and field-aligned current models are used together to derive the Poynting flux, without need for conductivity values. The Joule heating values are assumed to be the same as the Poynting flux. The model described in this paper was an interim version, replaced by a later version [Weimer, 2005a]. This model is constructed in similar manner as the 2001 version [Weimer, 2001], except that spherical cap harmonic analysis functions are used, and a different saturation formula is applied. The model uses solar wind inputs (density N , velocity V_x , and magnetic field B_y , B_z) and date and time to calculate the dipole tilt angle. Optionally, the AL index may be provided. Run 1_WEIMER results were provided by the modeler (D. R. Weimer), calculated at positions directly along the path of the DMSP satellite, with the exception of event 2 in December 2006, the "AGU Storm." The optional AL index values were not used. In the 1_WEIMER calculations, the IMF values were first propagated to the bow shock, using a time delay correction based on a minimum variance method [Weimer and King, 2008]. Averages of the measured solar wind values over the 16 min preceding each DMSP measurement were used for the model's input.

The CCMC recently implemented the 2005 Weimer electrodynamics model [Weimer, 2005a] which includes the electric potentials, field-aligned currents, and Poynting flux as outputs. Run 7_Weimer are Joule heat results obtained from the model using solar wind and AL values as input, and run 8_WEIMER was run without AL inputs. Solar wind data in the CCMC implementation are propagated using the 1 min solar wind speed from ACE's position to Earth assuming perpendicular phase fronts. Solar wind parcels that are passed by faster parcels are deleted and the resulting solar wind time line is interpolated back to a 1 min time cadence. No delays or further averaging are applied. Joule heat maps are derived from large-scale electric field and field-aligned current patterns and were generated on a 1 min time cadence and a grid with 0.5° latitude and 2° longitude resolution. The map data were then used to obtain interpolated values along the DMSP-F15 satellite track on a 5 s time cadence.

4.3.2. Cosgrove (1_Cosgrove and 2_Cosgrove)

The Cosgrove Poynting flux model ("Cosgrove PF" or "Cosgrove" hereafter) is specifically designed to provide Poynting flux (PF) values in that the statistical model was fit directly to individual PF measurements using 5 years of FAST satellite observations (from 1997 to 2001) [Cosgrove et al., 2014]. The model development was inspired by the Weimer models, and thus, there are two flavors of the Cosgrove model that use the same solar wind inputs and optional AL index values in the same way as does the Weimer model at the CCMC.

Run 1_Cosgrove was generated using observed AL index values and 2_Cosgrove without AL . The centers of the equal-area bins described in Cosgrove et al. [2014] were used as grid positions with a latitude resolution between 1.1° (6° away from the poles) and 0.26° (closest to the equator, 45° away for the poles) and a constant longitude resolution of 1.8° .

5. Methodology

Before we describe the results we have to introduce the methodology that is available to model-data comparisons at the CCMC and the methods that have been used to obtain (integrated) values from the individual satellite passes in this paper.

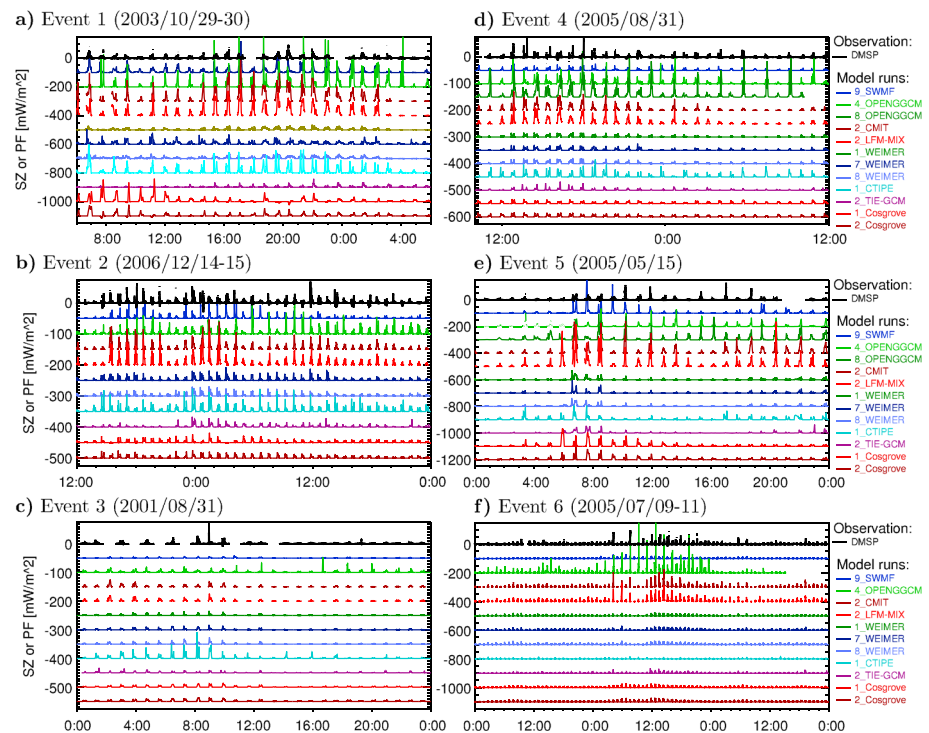


Figure 3. Overview plots of vertical Poynting flux (S_2 or PF) and Joule heat for the six events. Observations are shown with inverted sign ($-S_2$ positive means inflowing electromagnetic energy) in black with model results of Joule heat in stack-plot format below. The baselines shift between each run is -100 mW/m^2 for events (a) 1, (e) 5, and (f) 6 and -50 mW/m^2 for event (b) 2, (c) 3, and (d) 4. Events 4 (d) and 5 (e) have the full set of model runs. Events 1, 2, 3, and 6 are missing data for 8_OPENGGCM and event 2 also has no data for 1_WEIMER.

5.1. Skill Scores From Time Series

All observation and model results have been posted to the GEM and CEDAR metrics validation visualization on the CCMC web site and plots like the ones in Figure 3 can be generated online. Time series plots are primarily used for inspection and to identify individual agreement in the overall shape of an auroral zone encounter by the spacecraft and how this encounter is represented by the individual models. Figure 3 shows the observations and model results in a global overview plot for each event that roughly indicate the magnitude of Poynting flux and Joule heat or Poynting flux from the models through the course of each event. In each panel, the traces are separated from the observations (black, top) and each other by a constant offset (-100 mW/m^2 in events 1, 5, 6, and -50 mW/m^2 in events 2, 3, and 4).

Quantitative assessments of the skill of each model may use scores that have been developed for similar studies such as root-mean-square error, prediction efficiency, and correlation coefficient [Pulkkinen, 2011, 2013; Rastätter et al., 2013]. In this study, however, we take a different approach to the analysis of the model outputs that are based on individual passes of the auroral zone instead of on a global agreement between observation and model. The reason for this approach is that observations are changing on a timescale of less than a second with a large degree of variation. For comparison with models we average 10 s of the 1 s data to smooth the finest excursions while preserving the overall shape and amplitude of the signals during each pass.

5.2. Analysis of Each Pass

Each pass of the DMSP satellite through the auroral region is analyzed by dividing the pass into two segments, illustrated in Figure 4: The first segment begins when the satellite is within 45° of the magnetic pole (vertical dashed line in the left) and ends when the satellite reaches the point when it is closest to the magnetic pole (vertical dashed line in the middle). The second segment then begins and ends when the satellite has moved 45° away from that magnetic pole (vertical dashed line on the right). Each full satellite orbit has two passes through the auroral region (Northern and Southern Hemisphere), each with the two segments defined here. The observations are shown in black at the top and model traces are separated from the observation and each other by an offset of -50 mW/m^2 .

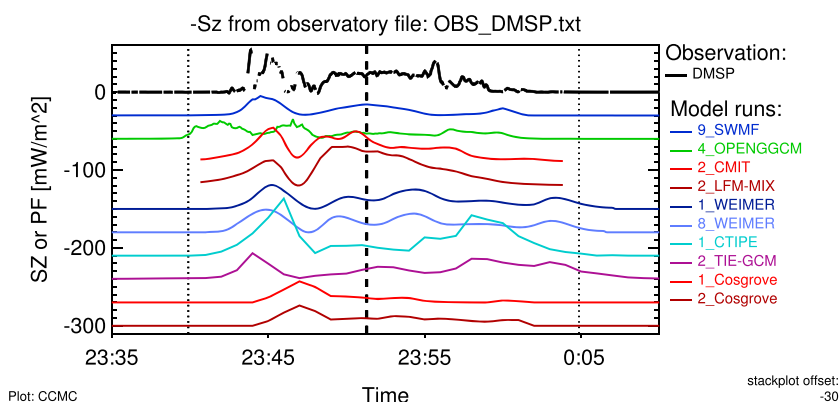


Figure 4. Sample pass during event 2 (10 s averaged data from Figure 2b). Stack plot of single auroral pass on 14 December 2006 23:35 to 15 December 2006 00:10 with 10 s averaged DMSP observations of the negative Poynting flux $-S_z$ (black) and model traces of Joule heat JH or Poynting flux (colors) with offset of -30 mW/m^2 between adjacent traces. The vertical dotted lines indicate the beginning and end time of the auroral pass (within 45° of the magnetic pole) and the dashed line in the center the closest approach to the magnetic pole. Model outputs for 2_CMIT and 2_LFM-MIX (red and brown colors in the middle) start later than the pass start time and end before the pass is complete because the ionosphere electrodynamics solver covers only the auroral region within 40° of the pole.

Although these individual passes are the essential element of this investigation, we are not able to display all of them in detail here in this paper. We refer to the online visualization that is available at the Community Coordinated Modeling Center (<http://ccmc.gsfc.nasa.gov>) that can be reached from the web page on the GEM-CEDAR metrics validation challenge.

Figure 5 shows two-dimensional Poynting flux or Joule heat distributions from some empirical model runs and radial field-aligned currents (JR) and Joule heat from coupled magnetosphere-ionosphere model runs. The Cosgrove Poynting flux model predicts a smaller auroral pattern than all the other models, resulting in PF peaks that are closer to the magnetic pole than the Joule heat peaks from the other models in Figure 4. Radial field-aligned current patterns (b: 4_OpenGGCM, c: 9_SWMF, and d: 2_LFM-MIX) determine the location and strength of horizontal currents in the ionosphere which lead to the modeled Joule heat patterns (panels f-h in the bottom row). The latitudinal size of the Weimer pattern in panel (e) is comparable to the patterns that are generated by the other models. However, between the coupled magnetosphere-ionosphere models OpenGGCM, SWMF, and LFM, different distributions of field-aligned currents result in considerably different Joule heat pattern. The OpenGGCM run exhibits Region 1 currents in the dayside and morning side as opposed to SWMF which has Region 1 and Region 2 currents of comparable strength in all quadrants (dayside/nightside and morning/evening side). The LFM run shows large Joule heat in the polar cap due to current closure from strong Region 1 currents in the dayside that are located at higher latitude than those for SWMF or OpenGGCM. In general, Joule heat in the coupled models is generated adjacent to inflowing and outflowing field-aligned currents. Joule heat calculated by the ionosphere electrodynamic models is especially concentrated between nearby layers of inflowing and outflowing currents of the same magnitude.

5.3. Skill Scores During the Course of Storms

During each auroral pass we compute the total track-integrated Poynting flux (shown in kW/m) and obtain the maximum value of PF and JH during the observations and each model run during the inbound segment (the satellite moves toward the magnetic pole) and outbound segment (satellite moves away from the pole) of the pass.

The ratio of the track-integrated values for model to observation is the integrated value yield (IYI). In contrast we also measure size and location of peak values using the amplitude yield (YI, referred to as “yield” later in the paper) that is the ratio of the modeled maximum and observed maximum value, and the timing error (DT, shown in minutes) that is the difference between the time of the maximum value in the model and the time of the observed maximum.

Figures 6–11 show the data that went into each average score during each of the six storms. Each figure has the same analyses: Integrated Poynting flux or Joule heat at the top (a) and (e), Yields in the middle ((b) and (f)), and timing errors below (c) and (g). To illustrate the progression of each storm, the D_{st} index is shown on the

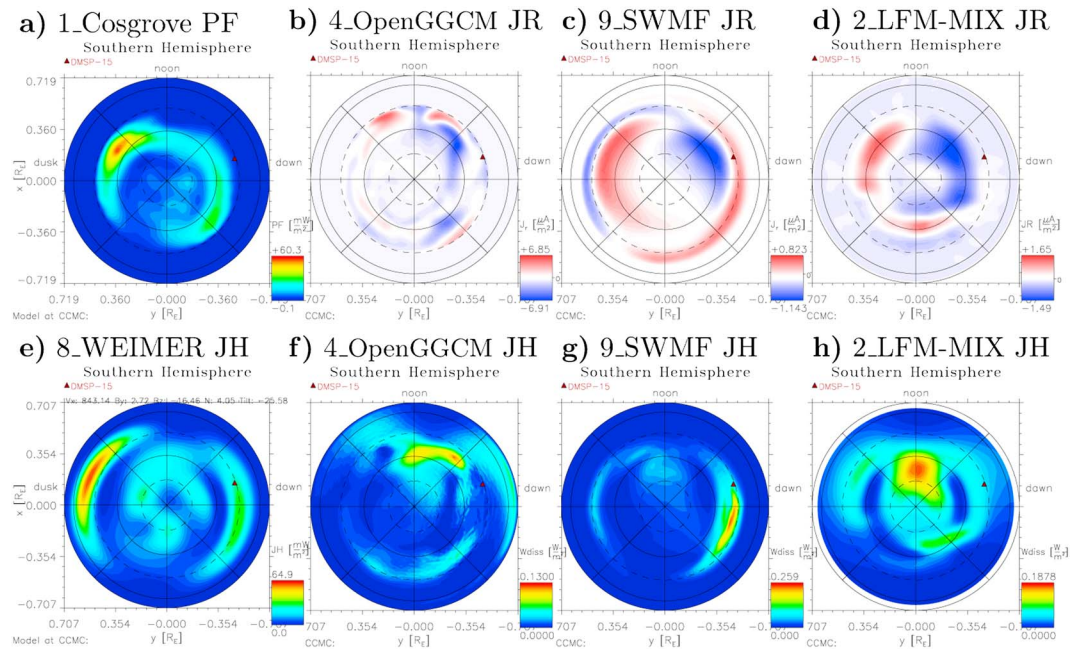


Figure 5. Poynting flux (PF), field-aligned (radial) currents (JR), and Joule heat (JH) from models at 23:45 UT on 14 December 2006 for the Southern Hemisphere. This figure shows two-dimensional patterns returned by statistical and coupled magnetosphere-ionospheric models at the time when the first maximum of PF was observed in the sample pass of Figure 4. (a) PF from 1_Cosgrove, (b–d) field-aligned currents (JR) from 4_OpenGGCM, 9_SWMF, and 2_LFM-MIX. (e) JH (Wdiss) from 8_WEIMER, 4_OpenGGCM, 9_SMF, and 2_LFM-MIX. The DMSP-15 satellite position at that time is indicated by a small triangle at about minus 60° magnetic latitude and 07:15 magnetic local time in the morning side. Color scales are different in each panel due to the different magnitudes specified by each model. Cosgrove PF and Weimer JH are in mW/m² as opposed to JH (Wdiss) values in W/m² in the panels for OpenGGCM, SWMF, and LFM.

left bottom (d) and AL on the right (h). The estimated 2 sigma error level for each pass are shown as grey color bars behind the observed integrated Poynting flux values in panels (a) and (e) and as intervals around the logarithmic yield (using base-2 logarithm I_d) in (b) and (f).

The segments described above for the different passes are combined by magnetic local time sector as we plot results and compute averages and standard deviations of skill scores: The inbound segments in the Northern Hemisphere and outbound segments in the Southern Hemisphere (all in the evening side between 20:00 and 22:00 MLT) contribute to skill scores plotted with asterisks in (b), (c), (f), (g) and listed with subscript 1 in Table 3. Averages and standard deviations have been calculated using only passes where the integrated observed Poynting Flux exceeds the 2 sigma error level. The outbound pass segments in the north and inbound segments in the south (in the morning side between 06:00 and 10:00 MLT are rendered with diamonds in (b), (c), (f), and (g) and are listed with subscript 2 in the table.

6. Results

The models show a large scatter that mostly falls outside the estimated uncertainty in the observational data indicated by vertical error bars (25% relative error) in the integrated Poynting flux and Joule heat in (a) and (e). The physics-based models show a larger spread in terms of integrated values and yield, compared to the empirical models which mostly show integrated values comparable to the observed values and yields below 1 ($I_d(YI) < 0$). Of the two physics-based models of the ionosphere, the TIEGCM model tended to have yields below 1 ($I_d(YI) < 0$) while CTIPe tended to have Yields above 1 ($I_d(YI) > 0$). Especially Joule heat derived from the ionospheric electrodynamics of magnetosphere MHD models are mostly above the observations (all OpenGGCM runs, most CMIT-LFM runs, and a few SWMF runs). For LFM, this is in agreement with the observation that the model tends to overestimate electric potentials (cross polar cap potentials) in certain conditions and thus electric fields, currents, and Joule heat [Slinker et al., 1999; Wiltberger et al., 2009]. SWMF sees realistic magnitudes of electric potentials and this is reflected in the Yields being around unity ($I_d(YI) \sim 0$).

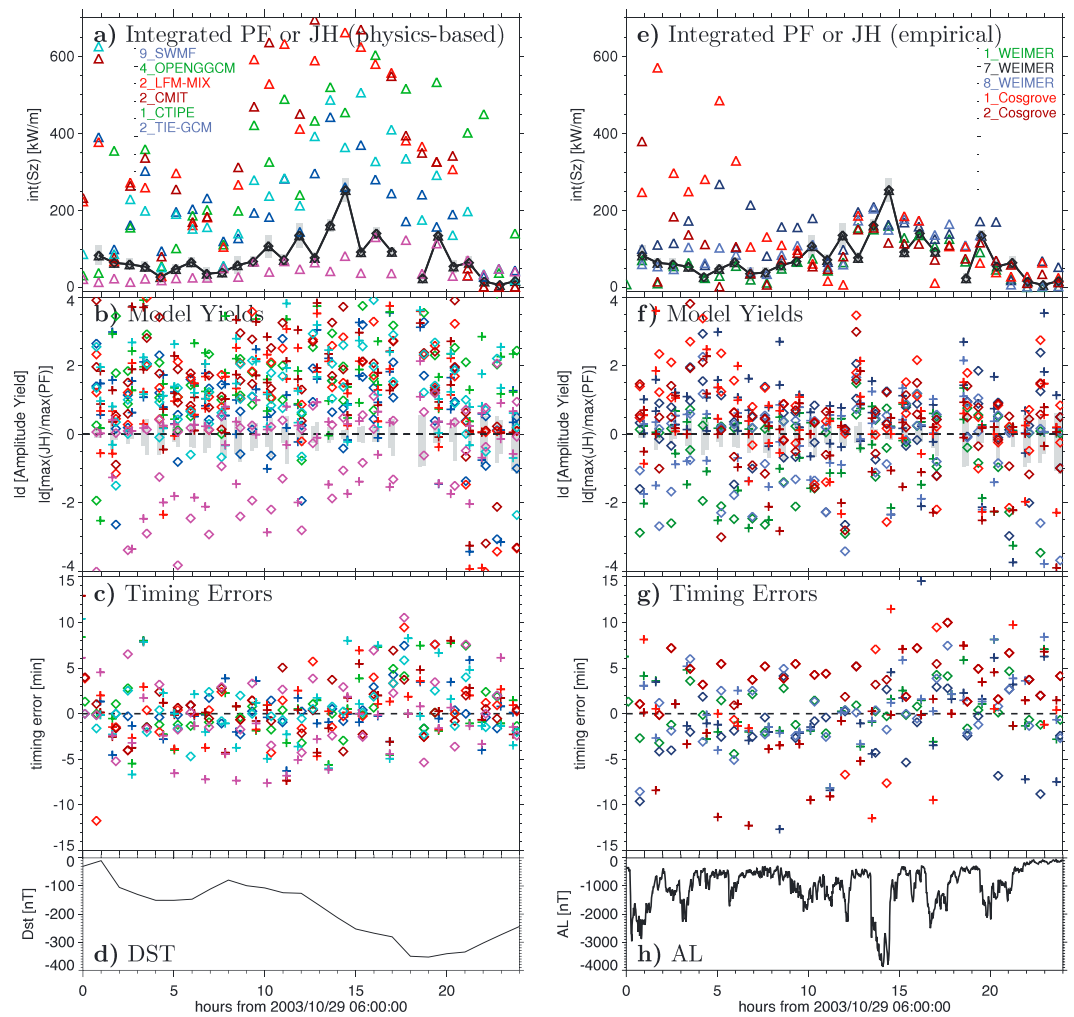


Figure 6. Summary of integrated values over auroral passes for event 1: (a–d) Physics based and (e–h) empirical models. (a–c) Scores for physics-based models: (a) Poynting flux or Joule heat integrated over full auroral passes (black symbols connected with black solid line are observations), ratio of model values to observed values constitute the Integrated value Yield (IYI). (b) Model Amplitude Yields YI (maximum Poynting flux or Joule heat divided by observed maximum Poynting flux) shown in base 2 logarithmic (\log_2) scaling for two pass segments (diamonds: evening side and crosses: morning side); in this scaling $\log_2(1) = 0$ is the perfect score. (c) Timing errors of maximum signal (time of model maximum minus time of observed maximum) for two segments of each pass of auroral region (symbols denote the same pass segments as Figure 6b). (d) D_{st} index, e–g: Scores for empirical models: (e) Integrated Poynting flux or Joule heat, (f) amplitude yields, (g) timing errors, and (h) AL index.

Table 3 shows the numerical scores obtained for each event for each model run and also as a summary across all events. The Halloween storm (event 1) is an unusual event in two respects: It was very strong and solar wind plasma data were reconstructed using low-temporal resolution velocity data and plasma density data from the Plasma Wave instrument on the Geotail spacecraft [Skoug *et al.*, 2004]. As a consequence, results from that event in the plots and the summary table should be taken with caution. Global magnetosphere models SWMF, OpenGGCM, CMIT, and LFM-MIX, as well as the ionosphere model CTIPE and the empirical Cosgrove model show very high yields that are not found for any other event. Yields for the remaining models are also higher than in the other events. Event 3 was a very weak event: SWMF shows very weak signals with an integrated yield of only $IYI = 0.12$ and Amplitude Yields $YI_1 = 0.04$ (evening side) and $YI_2 = 0.25$ (morning side). OpenGGCM and LFM also have lower integrated value yields (all values are 0.78 or lower) than in other events (integrated value yields are 0.99 and higher). Timing error averages are not significantly away from zero (given their large spread throughout each event, even when taking inbound and outbound segments separately).

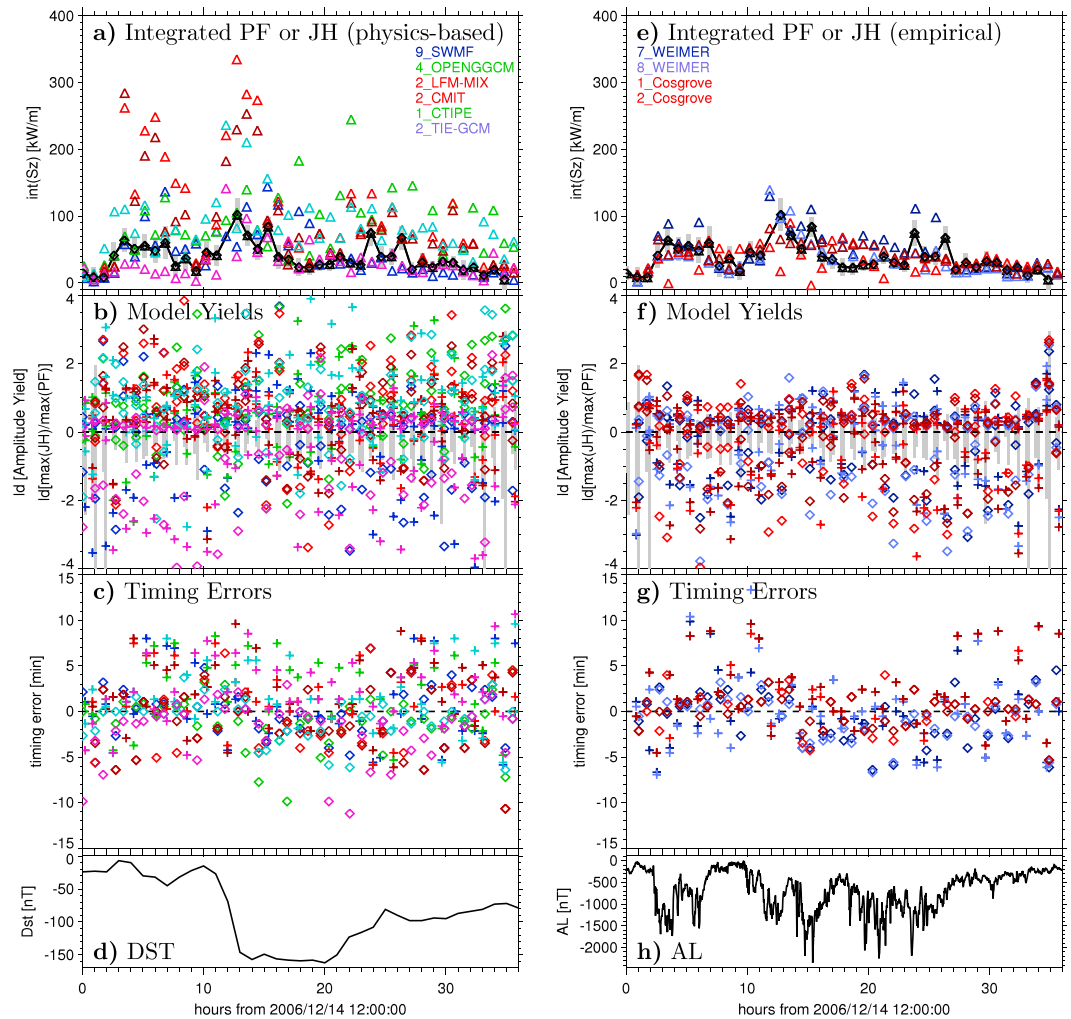


Figure 7. Summary of integrated PF and JH values over auroral passes for event 2: (a–d) Physics-based models and (e–h) empirical models with D_{st} and AL index values at the bottom. Results are in the same format as Figure 6. This event spans 1.5 days (36 h).

Plots of timing errors (panels c and g in the Figures 6 through 10) show that modeled maxima of Joule heat (physics-based models in panels c) and Poynting flux (empirical models in panels g) may occur randomly before or after the observed peak Poynting flux value. Sometimes, there seems to be a systematic shift toward the morning side (modeled peaks occur earlier in both segments) or the evening side (modeled peaks occur later than observed peaks). At other times the model may see an expanded structure (e.g., the morning side peak occurs earlier, the evening side later in the Northern Hemisphere, or the modeled evening side peak occurs earlier in the south with the morning side peak later than the observations). However, there is no discernible patterns that may indicate a consistent tendency toward larger or smaller modeled spread between peaks throughout any of the events and a shift during the course of any of the events. Empirical models show a slightly smaller spread in timing errors compared to the physics-based models. The maximum magnetic latitude encountered during each pass changes all the time as the Earth's magnetic field rotates underneath the orbital plane which is roughly constant in inertial coordinates from one orbit to the next. No correlation was found between timing errors and maximum magnetic latitude of each orbit for any of the models and any event.

All physics-based models, regardless of numerical approach, place Joule dissipation primarily at high latitudes (more than 45° from the magnetic equator): For example, during Event 2 (14–16 December 2006), run 9_SWMF model assigns only between 4% and 10% of the total Joule dissipation to lower latitudes, namely, ~ 105 GW out of a total of ~ 1.1 TW late on 14 December and ~ 65 GW out of ~ 1.4 TW early on 15 December.

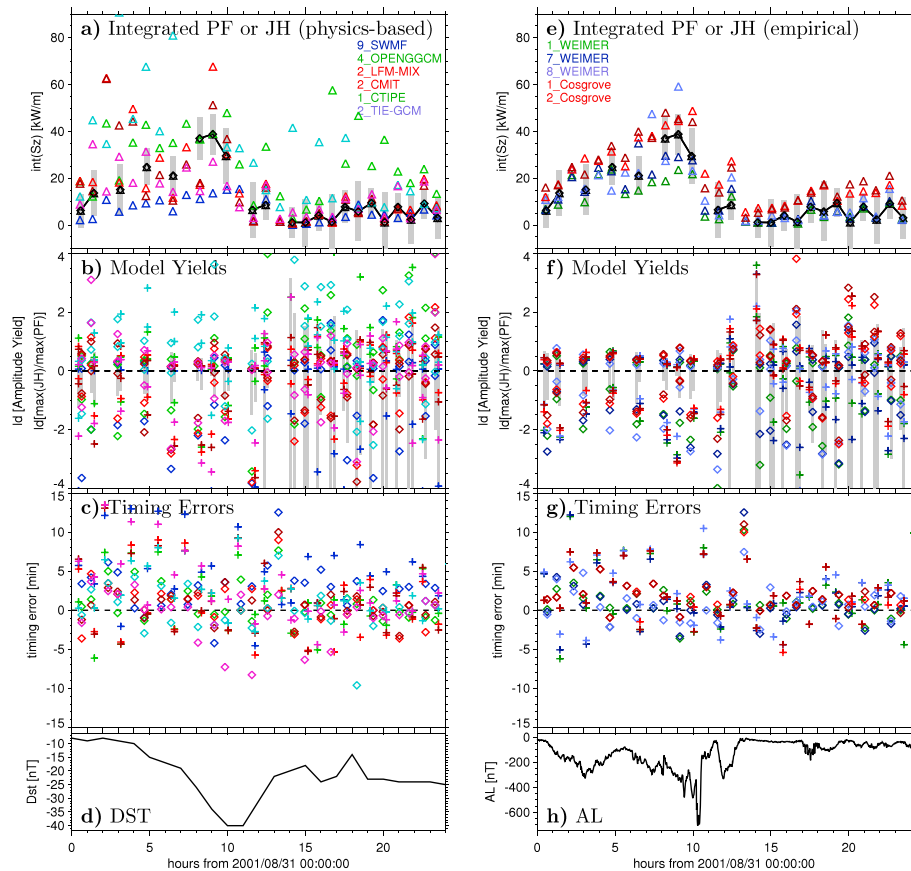


Figure 8. Summary of integrated PF and JH values over auroral passes for event 3: (a–d) Physics-based models and (e–h) empirical models with D_{st} and AL index values at the bottom. Results are in the same format as Figure 6. Summary of integrated PF and JH values over auroral passes for event 3: Physics-based models (Figures 6a–6d) and empirical models (Figures 6e–6h) with D_{st} and AL index values at the bottom. Results are in the same format as Figure 6.

Run 4_OpenGGCM assigns between 1.3% and 2.0% during the main phases of the storm (~20 GW on a level of ~1.5 TW late on 14 December and ~40 GW on ~2.0 TW early in 15 December). Run 2_TIE-GCM assigns between 0.7 and 1.6% (~10 GW out of ~1.5 TW and ~25 GW out of ~1.6 TW) and 1_CTIPe about 2.4% (~35 GW out of 1.5 TW at the storm’s peak in early 15 December). Runs of the LFM model (2_LFM-MIX and 2_CMIT) do not provide nonzero estimates of low-latitude Joule heat since the electrodynamics solver only extends up to 40° from the poles.

7. Discussion

Validation studies that measure model performance using quantitative skill scores have now become commonplace in the space physics community. The study presented here is the first comparison of observed energy influx (Poynting flux) in high latitudes and locally generated Joule heat from a wide variety of first-principles models together with a study of several Poynting flux models.

The comparison of models that calculate Joule dissipation with observations that result in in situ Poynting fluxes into the ionosphere shows that in general the modeled dissipation rates are similar in amplitude and location to the inflowing electromagnetic energy. We have calculated total Joule dissipation over the whole globe, and separately at high magnetic latitudes above 45°, and found that only a small fraction is dissipated at low latitudes. This strongly supports the assumption that incoming Poynting flux is dissipated at similar (high) latitudes.

Models that have been known to overestimate electric potentials and fields in the ionosphere during strong storm events such as OpenGGCM and LFM show larger Joule Dissipation rates compared to the incoming

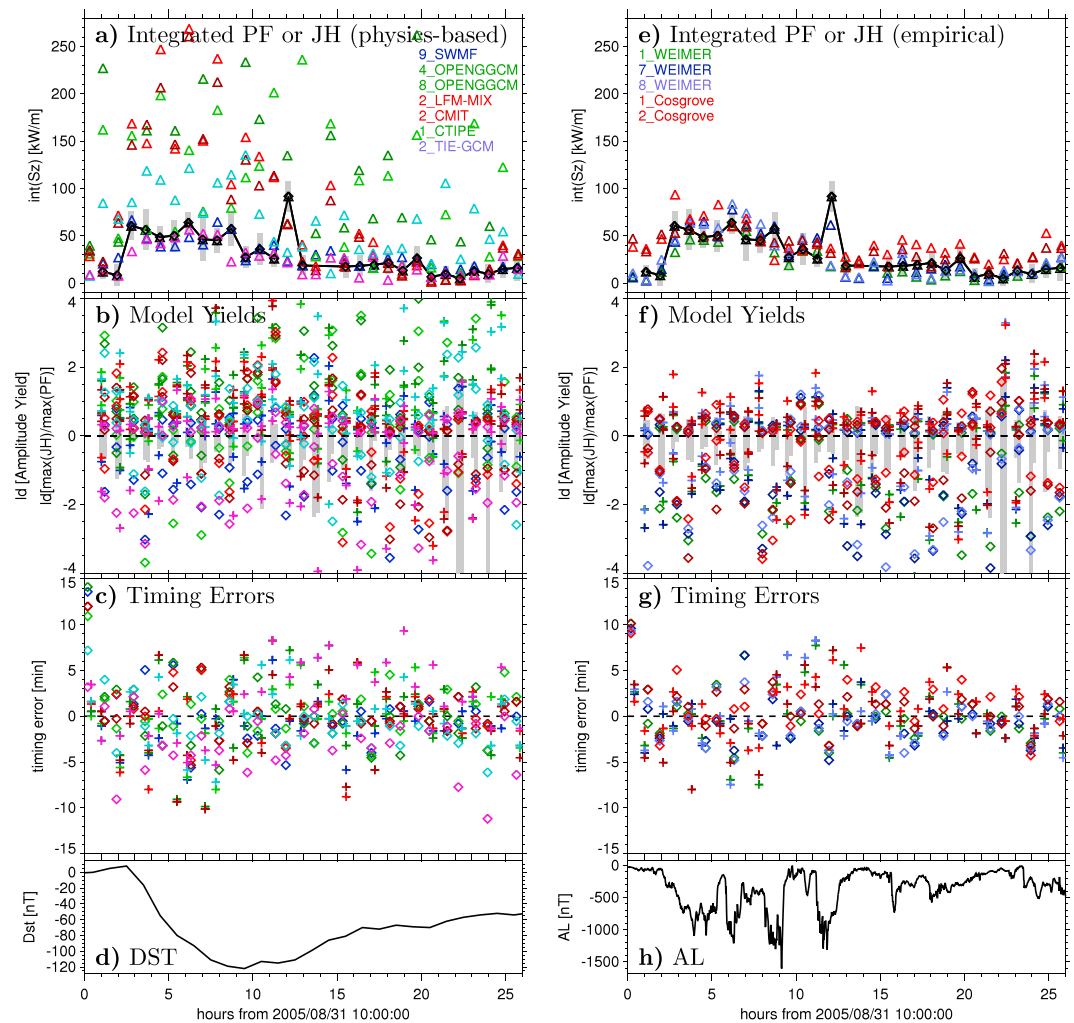


Figure 9. Summary of integrated values over auroral passes for event 4: (a–d) Physics-based models and (e–h) empirical models with D_{st} and AL at the bottom. Results are in the same format as Figure 6. This event spans 1.5 days (36 h). This event spans 1 day and 2 h (26 h).

Poynting flux. Other models that tend to predict weak electric potentials and currents, such as SWMF simulations with moderate magnetosphere resolution, show weaker Joule Dissipation than incoming Poynting fluxes (Yield < 1).

Overall, for each model tested we find a large spread of yields across the six events that were studied and a consistent relation between Poynting flux and Joule Dissipation could not be established because the standard deviation is comparable to the average Yield. Further studies are needed to address how similar Poynting flux and Joule dissipation patterns should be, i.e., whether there are significant energy transport mechanisms that may spread electromagnetic energy away from the point of entry into the ionosphere at the DMSP orbit at about 900 km altitude before that energy is converted into heat (Joule dissipation) at a much lower altitude (of about 100 km). First-principles models are only able to specify large-scale electromagnetic fields and are ill equipped to predict small-scale energy fluxes and dissipation patterns [Codrescu et al., 2000; Deng and Ridley, 2007].

Another aspect of model validation studies is grid convergence which has not been studied extensively. It is known that finer grid resolution can result in larger Joule heat estimates in three-dimensional ionosphere models [Deng and Ridley, 2007]. However, finer resolution may not necessarily result in better agreement between Joule heat and Poynting flux due to other forms of energy contributing to heating

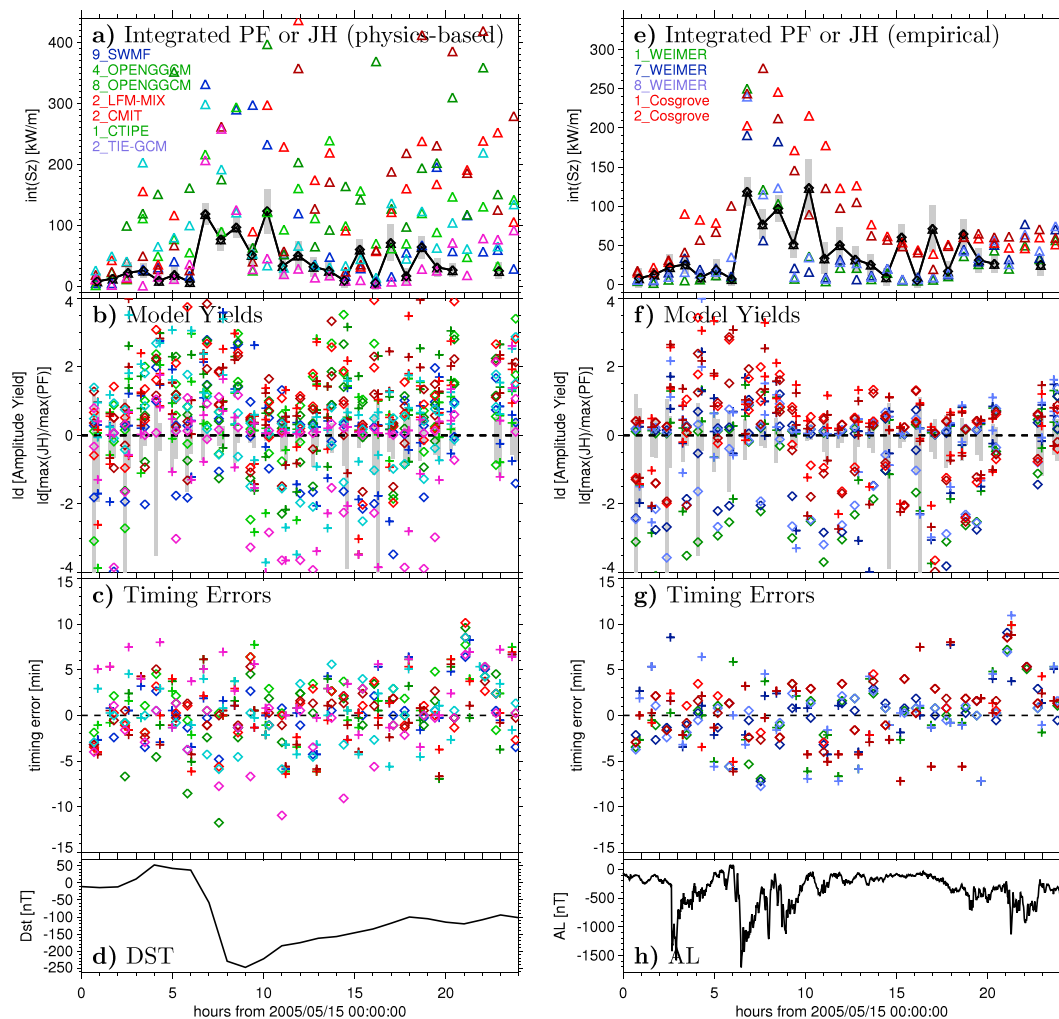


Figure 10. Summary of integrated values over auroral passes for event 5: (a–d) Physics-based models and (e–h) empirical models with D_{st} and AL at the bottom. Results are in the same format as Figure 6.

(such as neutral wind driving) and incoming electromagnetic energy (Poynting flux) being distributed to other regions in the ionosphere [Richmond, 2010; Vanhamäki et al., 2012]. The question whether a finer resolution model will yield results more similar to the observation, e.g., in terms of amplitudes and shape (width of peaks) will be left to future studies when model versions with significantly refined spatial resolution will be available for testing against the results from models used in this study. Improvements of spatial resolution should coincide with better temporal resolution as well as spatial scales of less than 200 km (about 2° latitude) are seen only with a Time resolution of less than 60 s (as used here for most models) [Gjerloev et al., 2011].

This study used Poynting flux results from a single DMSP satellite. The satellite’s orbit is Sun-synchronous, which means that in every orbit the satellite covers the same path in geographic latitude and geographic local time (azimuth angle seen from the Earth’s axis). In magnetic local time and magnetic latitude this translates to a swath of coverage that is restricted to about 2 h in magnetic local time (at the 45° distance from the magnetic poles) and about 20° in latitude at the closest approach to the magnetic pole. This band of spatial coverage may lead to selection effects where similar features are sampled in each orbit. The use of observations from multiple satellites during the same time may provide a fuller picture of each model’s behavior. With full magnetic local time coverage one may be able to obtain a comparison of the size of the polar region between each model and the observations. We did not find any correlation between the location of each pass through the auroral region and the skill scores calculated.

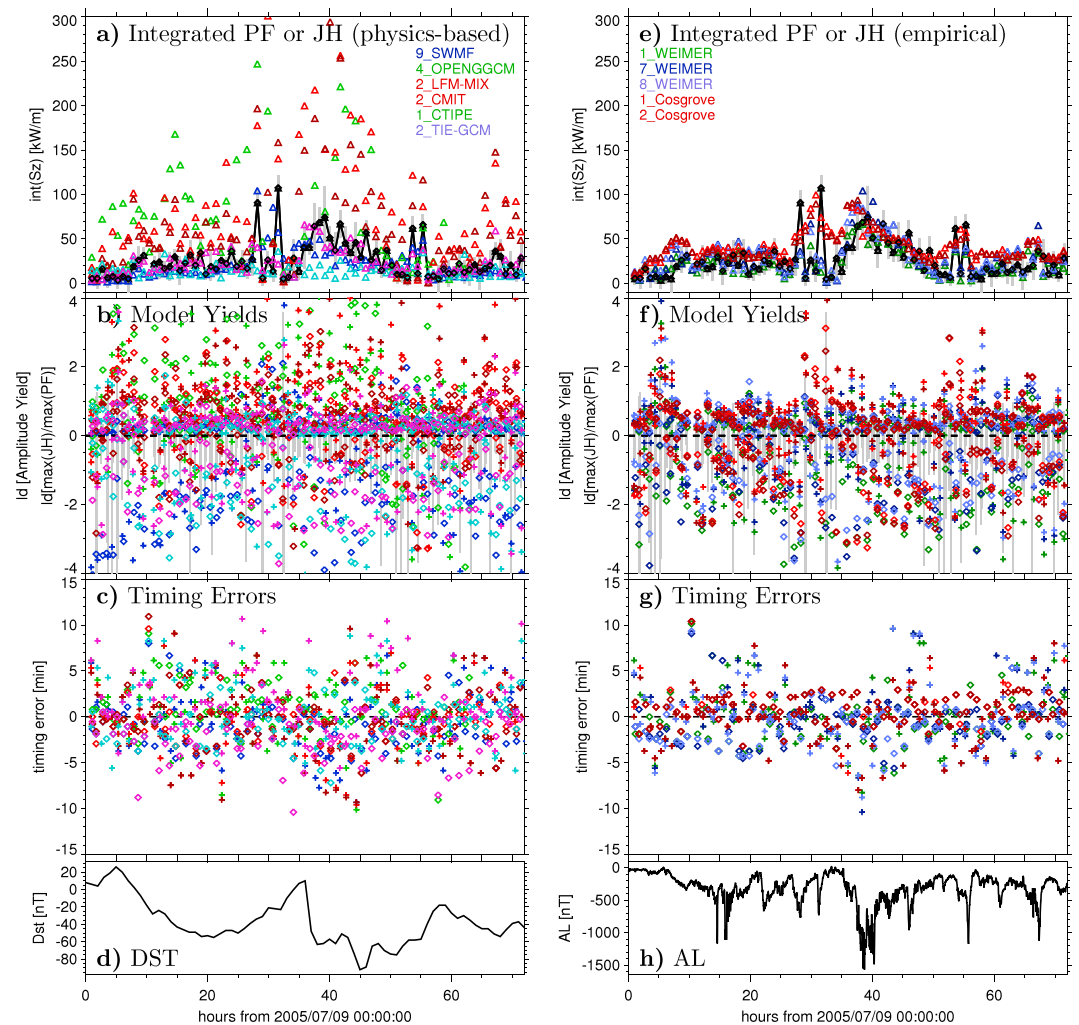


Figure 11. Summary of integrated values over auroral passes for event 6: Physics-based models (left) and empirical models (right) with D_{st} and AL at the bottom. Results are in the same format as Figure 6. This event spans 3 days (72 hours).

Yields vary strongly during each storm which comes from two effects. Poynting flux as measured by DMSP-F15 often varies strongly from one pass to the next, possibly sampling different areas in the auroral zone. Energy may get converted to neutral particle kinetic energy instead of Joule heat or kinetic energy of the neutral atmosphere may get converted back to electromagnetic energy, possibly reversing the sign of the Poynting flux during the late phase of a storm as driving from the magnetosphere decreases (flywheel effect). In these cases, direct comparisons between Poynting flux and Joule heat become meaningless. Further studies are needed to differentiate between storm phase and orbit location in magnetic coordinates.

8. Conclusions

Several models of the ionosphere thermosphere were run for six events defined during the 2008 GEM and the 2011 GEM-CEDAR challenges. Physics-based models include three-dimensional models of the ionosphere/thermosphere and two-dimensional ionospheric electrodynamics modules of global magnetosphere MHD models. Climatological models specify Joule heat from the electrodynamics of the ionosphere or the Poynting flux directly. DMSP observations were used to compute measured Poynting flux values (vertical component S_z), derived from in track and cross-track electric and magnetic fields. All model results were interpolated along the DMSP satellite track and timelines were analyzed in each pass of the auroral zone (i.e., satellite orbit segments within 45° of the northern and southern magnetic pole).

Table 3. Skill Score Values by Event and Summary for All Events^a

Run	YI	YI ₁	YI ₂	DT ₁ (min)	DT ₂ (min)	N	N _{an}
<i>Event 1</i>							
9_SWMF	1.60 ± 1.15	1.68 ± 1.10	1.73 ± 1.48	-0.02 ± 3.13	-0.41 ± 2.08	28	25
4_OPENGGCM	4.67 ± 4.74	4.06 ± 3.77	3.77 ± 3.45	0.09 ± 3.62	-0.19 ± 2.31	28	25
2_LFM-MIX	2.11 ± 1.64	1.98 ± 1.49	2.56 ± 1.66	-0.05 ± 3.36	0.03 ± 3.61	28	25
2_CMIT	2.54 ± 1.88	2.44 ± 1.78	3.17 ± 2.20	0.02 ± 3.47	0.37 ± 2.61	28	25
1_CTIPE	2.24 ± 1.48	2.47 ± 1.85	2.17 ± 1.74	0.10 ± 4.25	0.12 ± 1.98	28	25
2_TIE-GCM	0.47 ± 0.42	0.41 ± 0.26	0.42 ± 0.33	-2.71 ± 4.16	0.4 ± 3.76	28	25
1_WEIMER	0.36 ± 0.26	0.37 ± 0.25	0.42 ± 0.37	-0.30 ± 3.25	0.15 ± 2.22	28	25
7_WEIMER	0.98 ± 0.59	1.09 ± 0.69	0.93 ± 0.68	-0.75 ± 5.31	-1.34 ± 3.63	28	25
8_WEIMER	0.50 ± 0.35	0.56 ± 0.39	0.58 ± 0.52	0.36 ± 3.45	-0.29 ± 3.13	28	25
1_Cosgrove	1.23 ± 1.49	0.89 ± 1.30	1.73 ± 2.29	-0.83 ± 5.79	3.33 ± 5.12	28	25
2_Cosgrove	0.74 ± 0.66	0.45 ± 0.57	1.12 ± 1.07	-2.09 ± 5.28	3.87 ± 4.34	28	25
<i>Event 2</i>							
9_SWMF	0.73 ± 0.50	0.75 ± 0.69	0.92 ± 1.07	1.16 ± 4.15	0.44 ± 2.84	43	28
4_OPENGGCM	1.39 ± 0.93	1.29 ± 1.17	1.93 ± 1.75	2.86 ± 4.80	-0.95 ± 3.02	43	28
2_LFM-MIX	1.16 ± 0.73	1.10 ± 0.61	1.91 ± 1.77	2.70 ± 4.03	-1.88 ± 4.33	42	28
2_CMIT	1.07 ± 0.78	1.04 ± 0.68	1.77 ± 1.81	2.70 ± 4.63	-1.91 ± 3.80	42	28
1_CTIPE	1.30 ± 0.82	1.40 ± 1.08	1.48 ± 1.04	2.99 ± 4.36	-0.69 ± 2.41	43	28
2_TIE-GCM	0.42 ± 0.31	0.42 ± 0.32	0.64 ± 0.86	3.16 ± 4.51	-2.19 ± 4.13	43	28
7_WEIMER	0.56 ± 0.37	0.64 ± 0.40	0.62 ± 0.54	0.18 ± 3.99	-1.17 ± 2.72	42	28
8_WEIMER	0.51 ± 0.374	0.60 ± 0.40	0.54 ± 0.54	0.00 ± 4.31	-0.82 ± 2.35	42	28
1_Cosgrove	0.49 ± 0.36	0.47 ± 0.33	0.58 ± 0.58	1.77 ± 3.78	0.13 ± 2.33	42	28
2_Cosgrove	0.51 ± 0.32	0.53 ± 0.31	0.64 ± 0.53	1.93 ± 3.84	-0.08 ± 1.73	42	28
<i>Event 3</i>							
9_SWMF	0.12 ± 0.114	0.04 ± 0.02	0.25 ± 0.13	2.72 ± 3.79	1.98 ± 3.40	28	10
4_OPENGGCM	0.78 ± 0.67	0.69 ± 0.55	1.08 ± 1.19	0.23 ± 3.10	0.25 ± 1.13	28	10
2_LFM-MIX	0.45 ± 0.21	0.47 ± 0.24	0.53 ± 0.32	0.54 ± 2.80	0.37 ± 2.37	28	10
2_CMIT	0.46 ± 0.25	0.47 ± 0.30	0.53 ± 0.33	0.37 ± 2.86	0.05 ± 1.99	28	10
1_CTIPE	1.28 ± 0.75	1.35 ± 0.89	1.27 ± 1.08	1.54 ± 2.57	-0.73 ± 1.83	28	10
2_TIE-GCM	0.56 ± 0.36	0.59 ± 0.50	0.80 ± 0.86	2.34 ± 3.52	-1.03 ± 3.01	28	10
1_WEIMER	0.33 ± 0.18	0.35 ± 0.18	0.40 ± 0.19	0.41 ± 1.93	0.38 ± 2.03	28	10
7_WEIMER	0.35 ± 0.19	0.38 ± 0.20	0.40 ± 0.18	0.79 ± 2.61	-0.15 ± 2.19	28	10
8_WEIMER	0.43 ± 0.24	0.47 ± 0.18	0.47 ± 0.28	1.66 ± 3.09	-0.46 ± 1.95	28	10
1_Cosgrove	0.47 ± 0.22	0.48 ± 0.23	0.56 ± 0.22	0.24 ± 1.70	1.37 ± 1.81	28	10
2_Cosgrove	0.47 ± 0.22	0.49 ± 0.24	0.58 ± 0.23	-0.07 ± 2.06	1.35 ± 1.81	28	10
<i>Event 4</i>							
9_SWMF	0.54 ± 0.27	0.63 ± 0.30	0.49 ± 0.48	-1.19 ± 2.63	-0.45 ± 2.90	31	22
4_OPENGGCM	1.93 ± 1.76	2.12 ± 2.26	1.78 ± 1.83	-0.28 ± 3.91	0.69 ± 2.40	31	22
8_OPENGGCM	2.61 ± 2.62	2.33 ± 2.53	2.65 ± 2.41	0.01 ± 4.55	0.09 ± 2.67	29	20
2_LFM-MIX	0.99 ± 0.79	1.36 ± 0.96	1.11 ± 0.89	-1.32 ± 4.52	-0.45 ± 2.32	31	22
2_CMIT	0.89 ± 0.68	1.20 ± 0.81	1.01 ± 0.80	-1.71 ± 4.67	-0.56 ± 2.26	31	22
1_CTIPE	1.26 ± 0.83	2.04 ± 1.71	0.96 ± 0.59	0.22 ± 3.85	-0.53 ± 1.71	31	22
2_TIE-GCM	0.42 ± 0.21	0.61 ± 0.40	0.43 ± 0.33	0.87 ± 3.77	-2.32 ± 3.34	31	22
1_WEIMER	0.33 ± 0.18	0.53 ± 0.42	0.32 ± 0.25	-0.98 ± 3.15	-0.58 ± 2.11	31	22
7_WEIMER	0.37 ± 0.22	0.56 ± 0.43	0.36 ± 0.31	-0.41 ± 2.87	-0.62 ± 1.98	31	22
8_WEIMER	0.39 ± 0.23	0.65 ± 0.54	0.37 ± 0.32	-0.41 ± 3.33	-0.55 ± 2.34	31	22
1_Cosgrove	0.59 ± 0.25	0.86 ± 0.62	0.45 ± 0.24	1.03 ± 3.22	1.29 ± 2.47	31	22
2_Cosgrove	0.47 ± 0.24	0.71 ± 0.54	0.36 ± 0.24	-0.41 ± 3.74	0.73 ± 1.79	31	22

Table 3. (continued)

Run	IYI	YI ₁	YI ₂	DT ₁ (min)	DT ₂ (min)	N	N _{an.}
<i>Event 5</i>							
9_SWMF	1.16 ± 1.27	1.74 ± 2.71	0.87 ± 0.85	0.77 ± 3.18	-0.93 ± 2.10	28	21
4_OPENGGCM	1.31 ± 1.11	1.18 ± 0.92	1.26 ± 0.94	0.91 ± 4.38	1.64 ± 2.58	28	21
8_OPENGGCM	1.65 ± 1.47	2.43 ± 2.18	1.33 ± 1.05	1.00 ± 6.11	1.08 ± 3.26	25	17
2_LFM-MIX	2.37 ± 2.29	2.27 ± 2.01	2.75 ± 3.52	0.66 ± 3.65	0.06 ± 2.45	28	21
2_CMIT	1.86 ± 1.42	2.36 ± 1.67	1.73 ± 1.56	-0.46 ± 3.77	0.53 ± 1.87	28	21
1_CTIPE	1.24 ± 1.34	1.67 ± 1.62	0.82 ± 0.70	-0.29 ± 3.25	-0.60 ± 3.03	28	21
2_TIE-GCM	0.52 ± 0.65	0.55 ± 0.70	0.54 ± 1.03	3.07 ± 4.58	-1.53 ± 3.73	28	21
1_WEIMER	0.36 ± 0.36	0.56 ± 0.54	0.30 ± 0.33	-1.03 ± 3.69	-0.25 ± 2.44	28	21
7_WEIMER	0.45 ± 0.46	0.71 ± 0.71	0.34 ± 0.38	0.61 ± 3.98	-0.60 ± 2.28	28	21
8_WEIMER	0.48 ± 0.48	0.79 ± 0.96	0.36 ± 0.37	-0.29 ± 4.27	0.06 ± 2.24	28	21
1_Cosgrove	1.00 ± 1.13	1.35 ± 1.79	0.72 ± 0.54	-0.81 ± 4.01	0.97 ± 2.34	28	21
2_Cosgrove	0.80 ± 0.71	1.06 ± 1.07	0.64 ± 0.50	-0.71 ± 3.88	0.79 ± 2.46	28	21
<i>Event 6</i>							
9_SWMF	0.33 ± 0.27	0.37 ± 0.26	0.26 ± 0.18	-0.03 ± 3.97	-1.45 ± 2.80	84	51
4_OPENGGCM	2.21 ± 2.77	2.31 ± 2.60	2.14 ± 2.24	0.89 ± 4.17	0.79 ± 2.01	74	47
2_LFM-MIX	1.27 ± 0.87	1.70 ± 1.14	1.16 ± 0.71	-0.16 ± 4.73	-0.71 ± 2.68	84	51
2_CMIT	1.12 ± 0.71	1.53 ± 1.25	1.08 ± 0.69	-0.42 ± 4.54	-0.93 ± 2.48	84	51
1_CTIPE	0.34 ± 0.24	0.45 ± 0.35	0.28 ± 0.22	1.08 ± 3.80	-0.81 ± 2.68	84	51
2_TIE-GCM	0.43 ± 0.22	0.55 ± 0.43	0.43 ± 0.25	1.48 ± 3.91	-2.06 ± 3.05	84	51
1_WEIMER	0.39 ± 0.22	0.56 ± 0.44	0.36 ± 0.24	0.63 ± 3.25	-1.24 ± 2.48	84	51
7_WEIMER	0.48 ± 0.24	0.65 ± 0.41	0.46 ± 0.27	0.97 ± 3.41	-1.16 ± 2.19	84	51
8_WEIMER	0.55 ± 0.31	0.75 ± 0.59	0.50 ± 0.32	0.31 ± 3.36	-1.41 ± 2.28	84	51
1_Cosgrove	0.59 ± 0.36	0.76 ± 0.41	0.44 ± 0.29	-0.54 ± 3.13	0.75 ± 1.56	84	51
2_Cosgrove	0.56 ± 0.35	0.73 ± 0.45	0.41 ± 0.28	-0.46 ± 3.13	0.69 ± 1.54	84	51
<i>Summary for All Events</i>							
9_SWMF	0.73 ± 0.71	0.85 ± 1.14	0.73 ± 0.85	0.30 ± 0.99	-0.35 ± 2.69	242	157
4_OPENGGCM	2.23 ± 2.64	2.12 ± 2.35	2.14 ± 2.18	0.91 ± 1.37	0.36 ± 2.40	232	153
8_OPENGGCM	2.17 ± 2.17	2.38 ± 2.38	2.05 ± 1.92	0.49 ± 0.70	0.57 ± 2.97	54	37
2_LFM-MIX	1.44 ± 1.24	1.59 ± 1.23	1.69 ± 1.69	0.36 ± 1.28	-0.64 ± 3.17	241	157
2_CMIT	1.37 ± 1.08	1.58 ± 1.25	1.59 ± 1.41	0.07 ± 1.34	-0.64 ± 2.71	241	157
1_CTIPE	1.12 ± 0.92	1.38 ± 1.27	1.04 ± 0.95	0.99 ± 1.46	-0.57 ± 2.42	242	157
2_TIE-GCM	0.45 ± 0.36	0.52 ± 0.44	0.51 ± 0.62	1.29 ± 2.32	-1.60 ± 3.53	242	157
1_WEIMER	0.37 ± 0.25	0.50 ± 0.41	0.36 ± 0.28	-0.11 ± 0.72	-0.58 ± 2.33	199	129
7_WEIMER	0.55 ± 0.37	0.70 ± 0.50	0.54 ± 0.43	0.30 ± 0.72	-0.99 ± 2.57	241	157
8_WEIMER	0.50 ± 0.34	0.67 ± 0.58	0.49 ± 0.41	0.17 ± 0.51	-0.76 ± 2.43	241	157
1_Cosgrove	0.72 ± 0.78	0.80 ± 0.91	0.72 ± 0.99	0.06 ± 1.00	1.17 ± 2.78	241	157
2_Cosgrove	0.59 ± 0.45	0.68 ± 0.58	0.60 ± 0.55	-0.29 ± 1.23	1.10 ± 2.40	241	157

^aScores listed are average scores and standard deviations for each event: integrated value yield (IYI) is calculated for each pass, maximum value yield (YI₁ and YI₂) and timing error (DT₁ and DT₂) are derived separately for each pass segment (subscripts 1 and 2). The number of passes analyzed is N_{an.} out of N available for each run in each event. All values are also summarized for all events at the bottom. Pass segments 1 are in the evening side (18:00–22:00 h MLT) and segments 2 in the morning side (06:00–10:00 h MLT). Ideal yield values are 1 and ideal timing error values are 0.

Three measures of performance for physics-based models and empirical models were calculated. In each polar cap/auroral pass the track-integrated Poynting flux (in mW/m) is calculated and compared with modeled Joule heat or Poynting flux. From the plots we immediately see that the empirical models exhibit a smaller spread in terms of yield (Y_1, Y_2) ratio of maximum value of JH and PF. We also see the same behavior in terms of the ratio of integrated Joule Heat over integrated Poynting flux (YI). Timing errors are of the same order compared to the physics-based models. Empirical models have yields below 1 ($\ln(YI) < 0$) most of the time. Each model specifies changes in the size and shape of the aurora between quiet and disturbed times differently, resulting in timing errors. Yields and timing errors observed in individual passes do not change in a coherent way during the course of each storm event. We found no correlation between storm phase and sign or magnitude of timing errors for any of the models. Often we see a positive time error on one pass and negative values in the next pass for the same hemisphere and vice versa in rapid succession. The satellite samples roughly the same magnetic local time and magnetic latitude in subsequent passes. However, modeled patterns may appear earlier or later quickly, moving in an unpredictable manner. We organized the auroral pass segments by local time sectors to calculate the average skill scores. We found some shift in timing errors but no apparent correlation in terms of yields. We also do not discern a difference in behavior between Northern Hemisphere passes and Southern Hemisphere passes where the satellite orbit covers a larger range of magnetic latitudes and local times than in the north. Plots of scores arranged with maximum magnetic latitude (not shown) did not show any trends in an initial analysis.

Appendix A: Determination of Error Levels of DMSP Poynting Flux

There are three considerations in determining the uncertainty in the pass-integrated Poynting flux presented in this paper: (1) uncertainty associated with the DMSP measurements of horizontal ion drift components and horizontal magnetic perturbations that are deemed to be of good quality—quality flag (QF) = 1; (2) uncertainty associated with measurements of lesser quality; and (3) uncertainty arising from missing measurement components.

A1. Poynting Flux Uncertainty for Quality Flag = 1: Good DMSP Data

Here we estimate the uncertainty in Poynting flux under the assumption that all data from the DMSP retarding potential analyzer and the ion drift meter (IDM) have been designated as good quality: RQF = 1 and IQF = 1. The RPA provides along-track ion drift and the IDM provides cross track and vertical flows. When all of the horizontal data are QF = 1 we use the following standard expression for the absolute uncertainty in the field-aligned Poynting flux, S_z

$$\sigma_{S_z} = \frac{1}{\mu_0} \left[(\sigma_{dB_x} E_y)^2 + (\sigma_{dB_y} E_x)^2 + (\sigma_{E_x} dB_x)^2 + (\sigma_{E_y} dB_y)^2 \right]^{1/2}, \quad (A1)$$

where σ represents the uncertainty in the subscripted quantity, E_x and E_y represent the along- and across-track values of DMSP electric field, respectively, and dB_x and dB_y represent the magnetic perturbations along and across the DMSP track, respectively. The electric field components are derived from $\mathbf{E} = -\mathbf{v} \times \mathbf{B}$, where \mathbf{v} is the DMSP-measured ion velocity and \mathbf{B} is the geomagnetic field value at the spacecraft location. We need estimates for the uncertainties in these quantities. For moderate activity in the auroral zone [Knipp *et al.*, 2015] found that $\sigma_{dB_x} \sim \sigma_{dB_y} \sim 100$ nT. This value takes into account instrument uncertainty, spacecraft noise, uncertainty, in spacecraft location, etc. To estimate uncertainty in the electric field we use the following process:

1. Assume that horizontal \mathbf{v} and \mathbf{B} are perpendicular, ($|\mathbf{E}| = vB$) and further that both components of \mathbf{E} have the same uncertainty, then

$$\sigma_E = vB \left[(\sigma_v/v)^2 + (\sigma_B/B)^2 \right]^{1/2}. \quad (A2)$$

2. Assume $\sigma_E \sim \sigma_{E_x} \sim \sigma_{E_y}$

In equation (A2) we use a typical value of $B = 50,000$ nT as the average high-latitude Earth field and $\sigma_B \sim 100$ nT. A typical auroral zone ion velocity is 500 m/s. To estimate estimate σ_v we took all the QF = 1 ion drift data for the 18 days of the GEM-CEDAR challenge (both v_y and v_x), converted them into their log values,

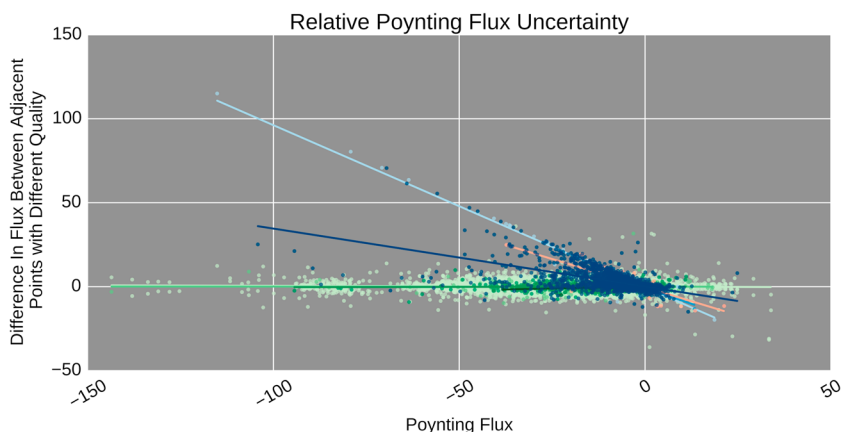


Figure A1. Example of Poynting flux change as Poynting flux quality flags (PQFQ) vary from point to point. Most of the point-to-point changes are small. However, when one of the ion drift velocity components is missing subsequent to a point with full measurements, we tend to find larger changes in calculated Poynting flux. X symbols in the IDM QF and RPA QF columns indicate absence of data from the respective instrument.

and determined the standard deviation of the log values. (We tested several different distributions; the log-normal distribution gave the best match to the distribution of the data). For both, it is about 200 m/s (note this value also includes the natural variability of the system, so it is probably an overestimate for the measurement uncertainty). Substituting the values into equation (A2) gives an uncertainty for E as: $\sigma_E \sim 10$ mV/m.

Using the ensemble of data for the three events investigated for this manuscript, we determined that typical auroral zone values of the field quantities were $E_x \sim E_y = 10$ mV/m and $dB_x \sim dB_y = 200$ nT. Putting all of the determined or estimated values into equation (A1) gives $\sigma_{S_z} \sim 2.5$ mW/m².

Since typical values of auroral zone Poynting flux are ~ 10 mW/m², we find that typical relative uncertainties in Poynting flux are (2.5/10) or $\sim 25\%$ if all of the ion drift data are of good quality. If the data have QF $\neq 1$, or if a component is missing, then additional uncertainty needs to be associated with the instantaneous value of the DMSP Poynting flux. We discuss these situations next.

A2. Poynting Flux Uncertainty With Quality Flag $\neq 1$

There is an additional uncertainty: The quality flags (xQFs) of the ion drift component data can have the following values: xQF1 = “usable,” xQF2 = “use with caution,” and xQF3 = “do not use.” Here “x” stands for either the RPA (R) data or IDM (I) data. Note that xQF = 3 data have not been used in this analysis. Additionally, there are data labeled as IQF4 = “unknown.” The IQF4 value is reported only for the DMSP IDM data and indicates that IDM drift values were obtained, but the attendant retarding potential analyzer (RPA) analysis failed for the 4 s analysis period. The RPA analysis can fail for a number of reasons. When hydrogen ions make up a large percentage of the plasma, one of the key assumptions for the RPA analysis is invalid, and thus, the processed RPA

Table A1. Estimate of Poynting Flux Variability With Point-to-Point Quality Flag Change^a

	IDM QF	RPA QF	Uncertainty	R	Line Color	# of Points
PFQF1	IQF1	RQF1	$-0.01S_z - 0.01$	-0.048	Pale green	574522
PFQF2	IQF2	RQF1	$0.01S_z + 0.00$	0.035	Light green	6763
PFQF3	IQF1	RQF2	$0.00S_z + 0.00$	-0.033	Med green	6032
PFQF4	IQF2	RQF2	$0.05S_z + 0.16$	0.323	Dark green	110
PFQF5	IQF1	x	$-0.93S_z - 0.17$	-0.966	Light blue	565
PFQF6	IQF2	x	$-0.96S_z - 0.52$	-0.961	Med blue	35
PFQF7	x	RQF1	$-0.59S_z - 0.24$	-0.808	Pink	177
PFQF8	x	RQF2	$-0.24S_z + 0.35$	-0.332	Red (not shown)	10
PFQF9	IQF4	x	$-0.36S_z + 0.04$	-0.657	Dark blue	9671

^aAn uncertainty of $\pm \Delta S_z$ is added to the reported S_z value. The right-most column shows the number of points for each category in the 18 days of the study. Colors listed are used in Figure A1. X symbols in the IDM QF and RPA QF columns indicate absence of data from the respective instrument.

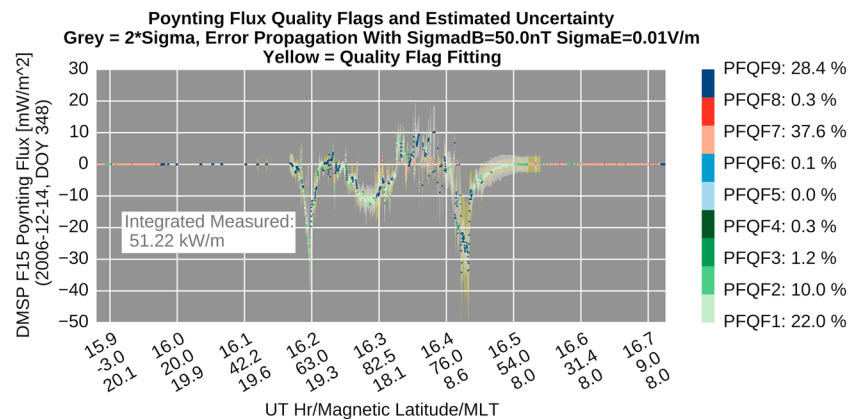


Figure A2. Calculated DMSP Poynting flux and associated uncertainty for a Northern Hemisphere pass beginning just before 16 UT on 14 December 2006. The dots show the calculated Poynting flux values. The yellow lines indicate the range of $\pm\Delta S_z$, which provides an estimate of relative uncertainty.

data will be reported as unusable. This frequently happens during solar minimum and/or winter conditions. Since the quality flags are based in part on the composition fraction, an RPA analysis failure results in the composition for that 4 s period not being recorded, which in turn triggers a report of IQF = 4 for the quality of the cross-track component of the ion drift, v_y .

During any given DMSP pass the quality of the ion drift data can change often, with high-quality data from either RPA or IDM juxtaposed with xQF data equal to 2 or 4. This introduces a significant uncertainty in the pass-integrated Poynting flux values (see Figure 2b). We have developed an objective, empirical method of assigning relative uncertainty to the Poynting flux and pass integrated Poynting flux based on the sequence of changes in quality flags. This method produces a Poynting flux quality flag (PRQF). The basis for this assignment comes from statistical analysis of all adjacent seconds of data where the first second has RQF = IQF = 1, and the subsequent second has a lower quality rating in either of the xQFs. For example, we start with instances where the RPA data and the IDM data have data with RQF = IQF = 1. This point would have PFQF = 1. At the next time step if the RPA has data with RQF = 1 and the IDM has data with IQF = 2 we assign as: PFQF = 2. If instead the RQF was equal to 2 and the IQF was equal to 2, then the Poynting flux flag would be assigned as PFQF = 4. A tabulation of PFQF values is shown in Table A1, columns 1–3.

For each event in which there was a change of quality flags between measurements we determine how much the calculated Poynting flux changed and store the information for further analysis. We found that large changes in quality flags between adjacent points were usually associated with large changes in Poynting flux, allowing us to do a fit to determine approximately how much Poynting flux change was associated with the changing quality flags. By fitting a line to the population of PFQF1 → PFQFn ($n = 1 \dots 9$) Poynting flux changes we can assign an additional uncertainty $\pm\Delta_{S_z}$ for each quality flag change. Thus, we determine a linear equation that expresses the estimated uncertainty in Poynting flux due to the subsequent point quality flag being QFn (see column 4 of Table A1). The results are shown in the top 4 rows of Table A1.

We perform a similar analysis for the situation in which one of the drift meter components is missing in the data files. The results are shown in the bottom four rows of Table A1. This estimated uncertainty can be significantly larger than the uncertainty in good quality data and therefore must be taken into account in the integrated flux uncertainty. Figure A2 shows the uncertainty range for a series of Poynting flux data points on 14 December 2006. The running sum of the largest value of $|S_z \pm \Delta_{S_z}|$ provides the total Poynting flux pass uncertainty.

References

- Bilitza, D., and B. W. Reinisch (2008), International Reference Ionosphere 2007: Improvements and new parameters, *Adv. Space Res.*, *42*(4), 599–609, doi:10.1016/j.asr.2007.07.048.
- Codrescu, M. V., T. J. Fuller-Rowell, J. C. Foster, J. M. Holt, and S. J. Cariglia (2000), Electric field variability associated with the Millstone Hill electric field model, *J. Geophys. Res.*, *105*, 5265–5273, doi:10.1029/1999JA900463.
- Cosgrove, R. B., et al. (2014), Empirical model of Poynting flux derived from FAST data and a cusp signature, *J. Geophys. Res.*, *119*, 411–430, doi:10.1002/2013JA019105.

Acknowledgments

DMSP data, outputs, and time series data from all models are available at the Community Coordinated Modeling Center (CCMC, <http://ccmc.gsfc.nasa.gov>). Follow the “Metrics and Validation” and “GEM-CEDAR Challenge” links. In the GEM-CEDAR challenge page, the link titled “Time series plotting tool (magnetosphere)” leads to a table (http://ccmc.gsfc.nasa.gov/challenges/GEM-CEDAR/plotting_tool_mag.php) with the events and physical quantities that were studied, including Poynting flux at the DMSP (F15) satellite. Solar wind input data for the models (magnetic field and plasma parameters) were obtained from CDAWeb (<http://cdaweb.gsfc.nasa.gov>). AL , K_p , and D_{st} index data are provided by the World Data Center for Geomagnetism in Kyoto, Japan (<http://wdc.kugi.kyoto-u.ac.jp>). D.J.K. and L.M.K. were partially supported by NASA grant NNX13AG07G. L.M.K. was also partially supported by NSF grant AGS 1144154. D.J.K. was partially supported by AFOSR award 12-091;FA9550-12*0264. The National Center for Atmospheric Research (NCAR) is supported by the National Science Foundation. The authors thank Art Richmond and Marc Hairston for their valuable discussions in improving the manuscript. The authors remember Kelly Ann Drake who prepared the DMSP data and got the effort started.

- Deng, Y., and A. J. Ridley (2007), Possible reasons for underestimating Joule heating in global models: E field variability, spatial resolution and vertical velocity, *J. Geophys. Res.*, *112*, A09308, doi:10.1029/2006JA012006.
- Fuller-Rowell, T., D. Rees, S. Quegan, R. J. Moffett, M. V. Codrescu, and G. H. Millward (1996), A coupled thermosphere-ionosphere model (CTim), in *STEP Report*, edited by R. W. Schunk, pp. 217, Scientific Communications on Solar Terrestrial Physics, Boulder, Colo.
- Gjerloev, J., S. Ohtani, T. Iijima, B. Anderson, J. Slavin, and G. Le (2011), Characteristics of the terrestrial field-aligned current system, *Ann. Geophys.*, *29*, 1713–1729, doi:10.5194/angeo-29-1713-2011.
- Gombosi, T. I., et al. (2014), Solution-adaptive magnetohydrodynamics for space plasmas: Sun-to-Earth simulations, *Comput. Sci. Eng.*, *6*, 14–35, doi:10.1109/MCISE.2004.1267603.
- Heelis, R. A., J. K. Lowell, and R. W. Spiro (1982), A model of the high-latitude ionospheric convection pattern, *J. Geophys. Res.*, *87*, 6339, doi:10.1029/JA087IA08p06339.
- Huang, C. Y., and W. J. Burke (2004), Transient sheets of field-aligned current observed by DMSP during the main phase of a magnetic superstorm, *J. Geophys. Res.*, *109*, A06303, doi:10.1029/2003JA010067.
- Knipp, D. J., S. Eriksson, L. Kilcommons, G. Crowley, J. Lei, M. Hairston, and K. Drake (2011), Extreme Poynting flux in the dayside thermosphere: Examples and statistics, *Geophys. Res. Lett.*, *38*, L16102, doi:10.1029/2011GL048302.
- Knipp, D. J., L. M. Kilcommons, J. Gjerloev, R. J. Redmon, J. Slavin, and G. Le (2015), A large-scale view of Space Technology 5 magnetometer response to solar wind drivers, *Earth Space Sci.*, *2*, 115–124, doi:10.1002/2014EA000057.
- Li, W., J. Raeder, and D. Knipp (2011), The relationship between dayside local Poynting flux enhancement and cusp reconnection, *J. Geophys. Res.*, *116*, A08301, doi:10.1029/2011JA016566.
- Lyon, J. G., J. A. Fedder, and C. M. Mobarry (2004), The Lyon-Fedder-Mobarry (LFM) global MHD magnetospheric simulation code, *J. Atmos. Sol. Terr. Phys.*, *66*, 1333–1350, doi:10.1016/j.jastp.2004.03.020.
- Merkin, V. G., and J. G. Lyon (2010), Effects of the low-latitude ionospheric boundary condition on the global magnetosphere, *J. Geophys. Res.*, *115*, A10202, doi:10.1029/2010JA015461.
- Millward, G. H., I. C. F. Müller-Wodarg, A. D. Aylward, T. J. Fuller-Rowell, A. D. Richmond, and R. J. Moffett (2001), An investigation into the influence of tidal forcing on F region equatorial vertical ion drift using a global ionosphere-thermosphere model with coupled electrodynamics, *J. Geophys. Res.*, *106*, 24,733–24,744, doi:10.1029/2000JA000342.
- Newell, P. T., T. Sotirelis, K. Liou, A. R. Lee, S. Wing, J. Green, and R. Redmon (2010), Predictive ability of four auroral precipitation models as evaluated using Polar UVI global images, *Space Weather*, *8*, S12004, doi:10.1029/2010SW000604.
- Powell, K. G., P. L. Roe, T. J. Linde, T. I. Gombosi, and D. L. De Zeeuw (1999), A solution-adaptive upwind scheme for ideal magnetohydrodynamics, *J. Comput. Phys.*, *154*(2), 284–309, doi:10.1006/jcph.1999.6299.
- Pulkkinen, A. (2011), Geospace environment modeling 2008–2009 challenge: Ground magnetic field perturbations, *Space Weather*, *9*, S02004, doi:10.1029/2010SW000600.
- Pulkkinen, A., et al. (2013), Community-wide validation of ground magnetic field perturbation predictions of geospace models to support model transition to operations, *Space Weather*, *11*, 369–385, doi:10.1002/2013SW000990.
- Raeder, J., J. Berchem, and M. Ashour-Abdalla (1996), The importance of small scale processes in global MHD simulations: Some numerical experiments, in *The Physics of Space Plasmas*, vol. 14, edited by T. Chang and J. R. Jasperse, MIT Cent. for Theoret. Geo/Cosmo Plasma Phys., Cambridge, Mass.
- Raeder, J., J. Berchem, and M. Ashour-Abdalla (1998), The Geospace Environment Modeling grand challenge: Results from a global geospace circulation model, *J. Geophys. Res.*, *103*, 14,787–14,797.
- Raeder, J., Y. Wang, and T. Fuller-Rowell (2001a), Geomagnetic storm simulation with a coupled magnetosphere-ionosphere-thermosphere model, in *Space Weather*, AGU Geophys. Mongr. Ser., edited by P. Song, G. Siscoe, and H. Singer, pp. 377–384, AGU, Washington, D. C.
- Raeder, J., et al. (2001b), Global simulation of the Geospace Environment Modeling substorm challenge event, *J. Geophys. Res.*, *106*(A1), 381–395, doi:10.1029/2000JA000605.
- Rastätter, L., M. M. Kuznetsova, A. Vapirev, A. Ridley, M. Wiltberger, A. Pulkkinen, M. Hesse, and H. J. Singer (2011), Geospace Environment Modeling 2008–2009 Challenge: Geosynchronous magnetic field, *Space Weather*, *9*, S04005, doi:10.1029/2010SW000617.
- Rastätter, L., et al. (2013), Geospace Environment Modeling 2008–2009 Challenge: D_{st} index, *Space Weather*, *11*, 187–205, doi:10.1002/swe.20036.
- Rastätter, L., G. Tóth, M. M. Kuznetsova, and A. A. Pulkkinen (2014), CalcDeltaB: An efficient postprocessing tool to calculate ground-level magnetic perturbations from global magnetosphere simulations, *Space Weather*, *11*, 553–565, doi:10.1002/2014SW001083.
- Rich, F. J., and M. Hairston (1994), Large-scale convection patterns observed by DMSP, *J. Geophys. Res.*, *99*, 3827–3844, doi:10.1029/93JA03296.
- Richmond, A. (2010), On the ionospheric application of Poynting's theorem, *J. Geophys. Res.*, *115*, A10311, doi:10.1029/2010JA015768.
- Richmond, A. D., E. C. Ridley, and R. G. Roble (1992), A thermosphere/ionosphere general-circulation model with coupled electrodynamics, *Geophys. Res. Lett.*, *19*, 601–604, doi:10.1029/92GL00401.
- Ridley, A. J., T. I. Gombosi, and D. L. De Zeeuw (2004), Ionospheric control of the magnetospheric configuration: Conductance, *Ann. Geophys.*, *22*, 567–584.
- Roble, R., and E. Ridley (1994), A thermosphere-ionosphere-mesosphere-electrodynamics general-circulation model (Time-GCM) – Equinox solar cycle minimum simulations (30–500 km), *Geophys. Res. Lett.*, *21*(6), 417–420, doi:10.1029/93GL03391.
- Roble, R., E. C. Ridley, A. D. Richmond, and R. E. Dickinson (1988), A coupled thermosphere / ionosphere general circulation model, *Geophys. Res. Lett.*, *15*, 1325–1328, doi:10.1029/GL015i012p01325.
- Schunk, R., L. Scherliess, and J. J. Sojka (2002), Ionospheric specification and forecast modeling, *J. Spacecr. Rockets*, *39*, 314–324, doi:10.2514/2.3815.
- Shim, J., et al. (2011), Cedar Electrodynamics Thermosphere Ionosphere (ETI) challenge for systematic assessment of ionosphere/thermosphere models: NmF2, hmF2, and vertical drift using ground-based observations, *Space Weather*, *9*, S12003, doi:10.1029/2011SW000727.
- Skoug, R. M., J. T. Gosling, J. T. Steinberg, D. J. McComas, C. W. Smith, N. F. Ness, Q. Hu, and L. F. Burlaga (2004), Extremely high speed solar wind: 29–30 October 2003, *J. Geophys. Res.*, *109*, A09102, doi:10.1029/2004JA010494.
- Slinker, S. P., J. A. Fedder, B. A. Emery, K. B. Baker, D. Lummerzheim, J. G. Lyon, and F. J. Rich (1999), Comparison of global MHD simulations with AMIE simulations for the events of May 19–20, 1996, *J. Geophys. Res.*, *104*, 28,379–28,395, doi:10.1029/1999JA900403.
- Toffoletto, F. R., S. Sazykin, R. W. Spiro, and R. A. Wolf (2003), Modeling the inner magnetosphere using the Rice Convection Model (review), *Space Science Reviews*, *WISER special issue*, *107*, 175–196, doi:10.1023/A:1025532008047.
- Tóth, G., et al. (2005), Space Weather Modeling Framework: A new tool for the space science community, *J. Geophys. Res.*, *110*(A12), A12226, doi:10.1029/2005JA011126.

- Tóth, G., et al. (2012), Adaptive numerical algorithms in space weather modeling, *J. Comput. Phys.*, 231(3,S1), 870–903, doi:10.1016/j.jcp.2011.02.006.
- Vanhamäki, H., A. Yoshikawa, O. Amm, and R. Fujii (2012), Ionospheric Joule heating and Poynting flux in quasi-static approximation, *J. Geophys. Res.*, 117, A08327, doi:10.1029/2012JA017841.
- Wang, W., T. L. Killeen, A. G. Burns, and R. G. Roble (1999), A high-resolution, three-dimensional, Time dependent, nested grid model of the coupled thermosphere-ionosphere, *J. Atmos. Sol. Terr. Phys.*, 61, 385–397, doi:10.1016/S1364-6826(98)00079-0.
- Wang, W., M. Wiltberger, A. G. Burns, S. C. Solomon, T. L. Killeen, N. Maruyama, and J. G. Lyon (2004), Initial results from the coupled magnetosphere ionosphere thermosphere model: Thermosphere-ionosphere responses, *J. Atmos. Sol. Terr. Phys.*, 66, 1425–1441, doi:10.1016/j.jastp.2004.04.008.
- Wang, W., T. L. Killeen, A. G. Burns, and R. G. Roble (2005), Initial results from the CISM coupled magnetosphere-ionosphere-thermosphere (CMIT) model: Thermosphere ionosphere responses, *J. Atmos. Sol. Terr. Phys.*, 66, 1425–1442, doi:10.1016/j.jastp.2004.04.008.
- Weimer, D. (2005a), Improved ionospheric electrodynamic models and application to calculating Joule heating rates, *J. Geophys. Res.*, 110, A05306, doi:10.1029/2004JA010884.
- Weimer, D. (2005b), Predicting surface geomagnetic variations using ionospheric electrodynamic models, *J. Geophys. Res.*, 110, A12307, doi:10.1029/2005JA011270.
- Weimer, D. R. (2001), An improved model of ionospheric electric potentials including substorm perturbations and application to the GEM November 24, 1996 event, *J. Geophys. Res.*, 106, 407–416, doi:10.1029/2000JA000604.
- Weimer, D. R., and J. H. King (2008), Improved calculations of interplanetary magnetic field phase front angles and propagation time delays, *J. Geophys. Res.*, 113, A01105, doi:10.1029/2007JA012452.
- Wiltberger, M., W. Wang, A. G. Burns, S. C. Solomon, J. G. Lyon, and C. C. Goodrich (2004), Initial results from the coupled magnetosphere ionosphere thermosphere model: Magnetospheric and ionospheric responses, *J. Atmos. Sol. Terr. Phys.*, 66, 1411–1423, doi:10.1016/j.jastp.2004.03.026.
- Wiltberger, M., R. S. Weigel, W. Lotko, and J. A. Fedder (2009), Modeling seasonal variations of auroral particle precipitation in a global-scale magnetosphere-ionosphere simulation, *J. Geophys. Res.*, 114, A01204, doi:10.1029/2008JA013108.
- Wolf, R. A., M. Harel, R. W. Spiro, G.-H. Voigt, P. H. Reiff, and C. K. Chen (1982), Computer simulation of inner magnetospheric dynamics for the magnetic storm of July 29, 1977, *J. Geophys. Res.*, 87, 5949–5962.